NASA/TM-2007-214607

Reentry Thermal Analysis of a Generic Crew Exploration Vehicle Structure

William L. Ko, Leslie Gong, and Robert D. Quinn
NASA Dryden Flight Research Center
Edwards, California

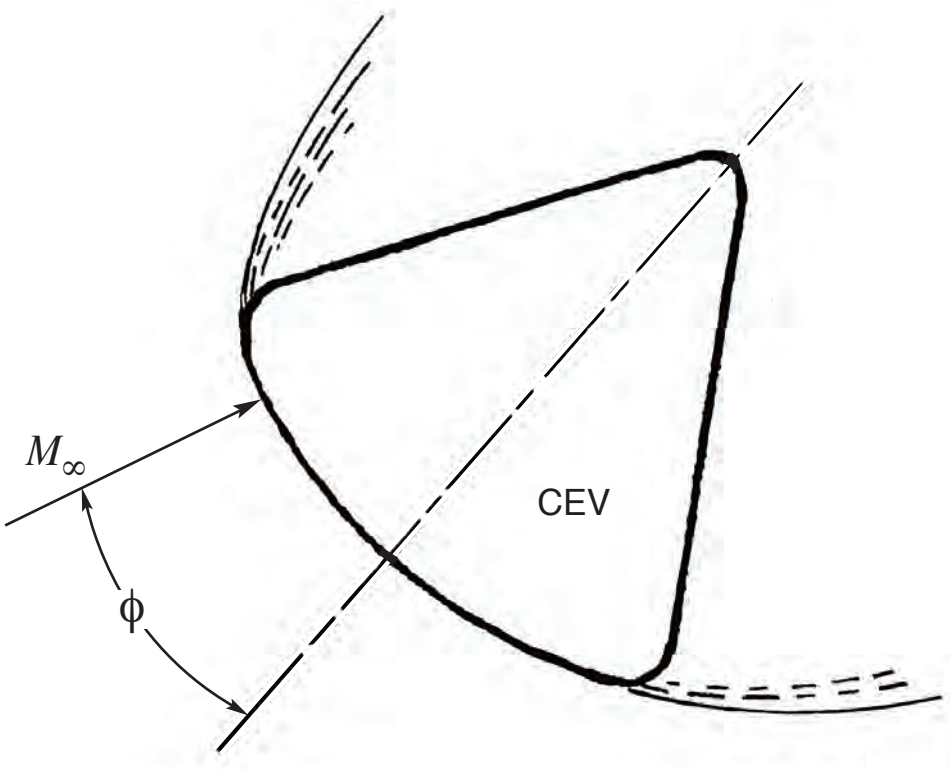

May 2007

NASA STI Program ... in Profile

Since its founding, NASA has been dedicated to the advancement of aeronautics and space science. The NASA scientific and technical information (STI) program plays a key part in helping NASA maintain this important role.

The NASA STI program is operated under the auspices of the Agency Chief Information Officer. It collects, organizes, provides for archiving, and disseminates NASA's STI. The NASA STI program provides access to the NASA Aeronautics and Space Database and its public interface, the NASA Technical Report Server, thus providing one of the largest collections of aeronautical and space science STI in the world. Results are published in both non-NASA channels and by NASA in the NASA STI Report Series, which includes the following report types:

- TECHNICAL PUBLICATION. Reports of completed research or a major significant phase of research that present the results of NASA programs and include extensive data or theoretical analysis. Includes compilations of significant scientific and technical data and information deemed to be of continuing reference value. NASA counterpart of peer-reviewed formal professional papers but has less stringent limitations on manuscript length and extent of graphic presentations.

- TECHNICAL MEMORANDUM. Scientific and technical findings that are preliminary or of specialized interest, e.g., quick release reports, working papers, and bibliographies that contain minimal annotation. Does not contain extensive analysis.

- CONTRACTOR REPORT. Scientific and technical findings by NASA-sponsored contractors and grantees.

- CONFERENCE PUBLICATION. Collected papers from scientific and technical conferences, symposia, seminars, or other meetings sponsored or cosponsored by NASA.

- SPECIAL PUBLICATION. Scientific, technical, or historical information from NASA programs, projects, and missions, often concerned with subjects having substantial public interest.

- TECHNICAL TRANSLATION. English-language translations of foreign scientific and technical material pertinent to NASA's mission.

Specialized services also include creating custom thesauri, building customized databases, and organizing and publishing research results.

For more information about the NASA STI program, see the following:

Access the NASA STI program home page at *http://www.sti.nasa.gov.*

- E-mail your question via the Internet to help@sti.nasa.gov.

- Fax your question to the NASA STI Help Desk at (301) 621-0134.

- Phone the NASA STI Help Desk at (301) 621-0390.

- Write to:
  NASA STI Help Desk
  NASA Center for AeroSpace Information
  7115 Standard Drive
  Hanover, MD 21076-1320

NASA/TM-2007-214607

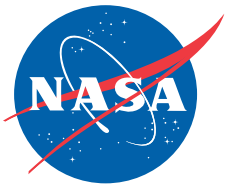

Reentry Thermal Analysis of a Generic Crew Exploration Vehicle Structure

William L. Ko, Leslie Gong, and Robert D. Quinn
NASA Dryden Flight Research Center
Edwards, California

National Aeronautics and
Space Administration

Dryden Flight Research Center
Edwards, California 93523-0273

May 2007

Cover art: NASA Dryden Flight Research Center, art number 070111.

Available from:

NASA Center for AeroSpace Information
7115 Standard Drive
Hanover, MD 21076-1320
(301) 621-0390

CONTENTS

ABSTRACT

Comparative studies were performed on the heat-shielding characteristics of honeycomb-core sandwich panels fabricated with different materials for possible use as wall panels for the proposed crew exploration vehicle. Graphite/epoxy sandwich panel was found to outperform aluminum sandwich panel under the same geometry due to superior heat-shielding qualities and lower material density.

Also, representative reentry heat-transfer analysis was performed on the windward wall structures of a generic crew exploration vehicle. The Apollo low Earth orbit reentry trajectory was used to calculate the reentry heating rates. The generic crew exploration vehicle has a graphite/epoxy composite honeycomb sandwich exterior wall and an aluminum honeycomb sandwich interior wall, and is protected with the Apollo thermal protection system ablative material. In the thermal analysis computer program used, the TPS ablation effect was not yet included; however, the results from the nonablation heat-transfer analyses were used to develop a "virtual ablation" method to estimate the ablation heat loads and the thermal protection system recession thicknesses. Depending on the severity of the heating-rate time history, the virtual ablation period was found to last for 87 to 107 seconds and the ablation heat load was estimated to be in the range of 86 to 88 percent of the total heat load for the ablation time period. The thermal protection system recession thickness was estimated to be in the range of 0.08 to 0.11 inches. For the crew exploration vehicle zero-tilt and 18-degree-tilt stagnation points, thermal protection system thicknesses of $h = \{0.717, 0.733\}$ inches were found to be adequate to keep the substructural composite sandwich temperature below the limit of 300°F.

NOMENCLATURE

a	thermal absorptivity
b_1	length of free side of honeycomb cross section, in.
c	height of spherical segment, in.
c_p	specific heat, Btu/lb-°F
C41	four nodes convection element
CEV	crew exploration vehicle
d_1	size of honeycomb cell (maximum diagonal of the cell cross section), in.
D	diameter, in.
FRSI	Felt Reusable Surface Insulation
h	TPS thickness, in.
h_c	honeycomb core depth, in.
JLOC	joint location (node)
k	thermal conductivity, Btu/s-in-°F
k_1, k_2, k_3	thermal conductivities in 1,2,3 directions, Btu/s-in-°F

k_L	thermal conductivity in fiber direction, Btu/s-in-°F
k_T	thermal conductivity normal to fiber direction, Btu/s-in-°F
K31	three nodes conduction element
K41	four nodes conduction element
K81	eight nodes conduction element
L/D	lift-to-drag ratio
msl	mean sea level
M_∞	free-stream Mach number
q_A	ablation heat load, Btu/in^2
q_C	conduction heat load for heating the virgin TPS and keeping it at the ablation temperature, T_A (this heat load includes the heat losses through external and internal radiation, heat loss through internal convection, and conduction), Btu/in^2
q_T	$= q_A + q_C$, total heat load for ablation period, Btu/in^2
q_V	heat of vaporization (including charring), Btu/lb
$\dot{q}$	heating rate, Btu/in^2-s
$\dot{q}_C$	heating rate to keep TPS surface temperature at 1200°F, Btu/in^2-s
$\dot{q}_{\text{Stag}}$	stagnation heating rate, Btu/in^2-s
r	diffuse component of the total reflectivity
r_c	radius of CEV wind-ward spherical wall, in.
R	radius, in.
R31	three nodes radiation element
R41	four nodes radiation element
S	radial distance, in.
STS	space transportation system
t	time, s
t_1	ablation starting time, s
t_2	ablation ending time, s
t_c	honeycomb cell wall thickness, in.
t_s	sandwich panel face sheet thickness, in.
T_A	ablation temperature, °F
T_s	surface temperature, °F
T_t	total or stagnation temperature, °F
T_{SW}	composite sandwich wall maximum temperature at touchdown, °F
TPS	thermal protection system
V_∞	free stream velocity, ft/s
W	windward TPS intact weight, lb

ΔW	vaporized TPS weight through ablation, lb
α_1, α_2, α_3, α_4, α_5	angles of attack, deg
δ	TPS recession layer thickness, in.
ε	thermal emissivity
θ	angular coordinate, deg
ρ	density, lb/in^3
ϕ	angle of tilt, deg

INTRODUCTION

The future crew exploration vehicle (CEV) is designed to carry a four-person crew for approximately 16 days during a lunar exploration mission. At the end of the mission, the CEV reentry capsule will return to the Earth, reentering the Earth's atmosphere and concluding the mission with a nominal landing on land as the baseline landing mode. The contingency plan will be a landing on water, similar to earlier Apollo cases. The geometry of the proposed CEV reentry capsule could be very similar to the shape of the earlier Apollo capsule or much larger. The CEV reentry capsule structures must be designed to survive the severe reentry aerodynamic heating and to mitigate the baseline landing impact by jettisoning the heat shield and deploying some type of shock absorbing system before landing.

Since the Apollo era, various new advanced materials have been developed, some of which are far more efficient (providing low density, light weight, high strength, and low heat conduction) than the structural shell materials that were used to build the Apollo capsule. Before beginning the construction of the proposed CEV reentry capsule, comparative studies of the heat-transfer characteristics and the mechanical performance of the candidate advanced materials must be performed to determine the best materials to use to build the capsule.

This report describes the studies that were performed to compare the heat-shielding characteristics of honeycomb-core sandwich panels fabricated with different materials, in order to determine the most promising candidate sandwich structure for the CEV windward wall structures.

Additionally, hypothetical reentry heat-transfer analyses were performed on a generic CEV reentry capsule windward wall structures covered with a thermal protection system (TPS). In the reentry thermal analysis, the effect of ablation on the TPS was not included because the ablation analysis computer program was not available. The main purpose of the hypothetical analysis was to study the effects of different heating rates on the substructural temperatures, and to provide some basic information for the design of the TPS of the future CEV. Nevertheless, the results (overall applied heat loads and the thermal response of the TPS and the substructures) obtained from the nonablation heat-transfer analysis were used to develop a "virtual ablation" approximation method to estimate the ablation heat loads and the TPS recession thicknesses.

This report presents the results of the heat shielding analysis of different honeycomb sandwich panels, the results of nonablation thermal analysis, and the graphical method developed for the virtual ablation analysis.

THE CREW EXPLORATION VEHICLE REENTRY CAPSULE

The geometry of the proposed CEV reentry capsule is shown in figures 1(a) and 1(b). The outer mold line shape of the capsule is essentially a modified larger version of that of the earlier Apollo capsule. The forebody (windward) outer surface is a shallow spherical cap with a 196.85 in. (5.00 m) diameter (compared to the 154.00 in. diameter of the Apollo capsule) and a 246.00 in. (6.25 m) radius of curvature (compared to the 184.80 in. radius of curvature of the Apollo capsule). The aft-body is a rounded cone with a 30.25° side wall angle (compared to the 33.00° side wall angle of the Apollo capsule) measured from the axis of symmetry. The apex of the aft-body cone is rounded. The proposed CEV reentry capsule is to reenter the Earth's atmosphere at an angle of tilt in order to achieve a hypersonic lift-to-drag ratio, L/D = 0.5, during reentry (compared to L/D = 0.3 for the Apollo capsule).

Figure 2 shows the reentry flight configuration of a generic CEV capsule at a ϕ degree angle of tilt. As the tilt angle ϕ increases, the stagnation point will migrate upward, and the heating rate will gradually increase from the zero-tilt spherical stagnation heating rate. Based on Apollo data (ref. 1), at ϕ = 18° angle of tilt, the local heating rate at the top toroidal shoulder could reach as high as 1.4 times the zero-tilt spherical stagnation heating rate.

The optimum (minimum) TPS thickness for the CEV windward spherical wall is determined based on the most severe heating rate among all possible heating rates associated with different reentry trajectories. In the present analysis, only the low Earth orbit reentry trajectory was considered. The optimum TPS thickness is defined as the TPS thickness that will protect the underlying composite sandwich wall from overheating beyond the limit temperature (300°F), and that will maintain the interior aluminum sandwich wall (of the crew compartment) at a comfortable temperature during the entire reentry flight.

Additionally, there exists a structural problem that must be considered in the development of the CEV capsule design. At the time of the landing impact (whether on water or on land), the shallow spherical shell will be bent inward if it is not properly reinforced on the interior side (fig. 2). This flattening bending will in turn bend the toroidal shoulder shell that joins the spherical shell and the aft-body conical shell, reducing the radius of curvature of the toroidal shell. It is well known that the bending of the curved sandwich shell in a direction reducing the radius of curvature will induce depth-wise compression in the honeycomb core. If the depth-wise compression is too severe, honeycomb cell wall can buckle, resulting in the collapse of the honeycomb core. Honeycomb cell wall buckling problems were extensively studied by Ko (ref. 2). Thus, the outer and inner shell of the crew compartment must be properly connected to improve structural rigidity.

THE APOLLO CAPSULE

Figure 3 shows the structure of the Apollo capsule, which was a double-walled sandwich construction. The windward spherical shell had a 184.80 in. radius. The fairing between the spherical segment and the conical segment is connected by a toroidal section having a 7.70 in. radius. The outer shell of the capsule (immediately beneath the TPS) was a sandwich shell fabricated with aluminum honeycomb core with steel face sheets at both sides. The inner shell was fabricated with aluminum honeycomb-core sandwich shell supported at discrete locations. The Apollo capsule was protected by the ablative TPS material Avcoat 5026-39/HC-G (a low-density glass-filled epoxy-novolac system) which had an ablation temperature of approximately 1200°F (ref. 3). Table 1 compares the thermal properties of the Apollo TPS and the Space Shuttle TPS tile at 1200°F.

Table 1. Comparison of thermal properties of the Apollo TPS and the Space Shuttle TPS tile at 1200°F (approximate ablation temperature).

TPS	ρ, lb/in^3	c_p, Btu/lb-°F	k, Btu/s-in-°F	ρc_p, Btu/in^3-°F	$k/(\rho c_p)$, in^2/s
Apollo	1.9097-2	0.655	0.3241-5	12.51-3	0.2591-3
Space Shuttle	0.5208-2	0.294	0.1754-5	1.53-3	1.1455-3

Table 1 shows that the Apollo virgin TPS was 3.67 times heavier than the Space Shuttle TPS tiles. In addition, it can be seen that the Apollo virgin TPS had 1.85 times the conductivity of that of the Space Shuttle TPS tile, and that the heat capacity, ρc_p, was 8.18 times that of the Space Shuttle TPS tile. Also shown in this table is the thermal diffusivity, $k/(\rho c_p)$. Thermal diffusivity is the ability of a material to absorb and prevent heat from penetrating to the structure; a lower numerical value indicates a higher capability to perform this function. As shown, the thermal diffusivity of the Apollo virgin TPS was less than that of the Space Shuttle TPS tile by a factor of approximately 4.42. Therefore, for a given thickness and temperatures of 1200°F or less, the Apollo virgin TPS was capable of absorbing more heat than the Space Shuttle TPS tile.

Figure 4 shows an Apollo low Earth orbit reentry trajectory (altitude, velocity) (ref. 1). Note that the Apollo reentry flight lasted for 374 s. For comparison, the Space Shuttle orbiter reentry flight STS-5 lasted for 1821 s which is 4.87 times longer (ref. 4).

Figure 5 (ref. 1) shows a typical wind-tunnel distribution of a local heating rate obtained for the Apollo capsule at ϕ = 18° angle of tilt, normalized by the measured zero-tilt (ϕ = 0°) stagnation point heating rate. Note that the heating rate at the top of the toroidal shoulder surface is almost 1.4 times higher than the zero-tilt stagnation point heating rate due to the local radius change at the stagnation point, which moved toward the upper toroidal shoulder for ϕ = 18° angle of tilt. Also, the heating rate at the bottom of the toroidal shoulder surface for ϕ = 18° angle of tilt is only 60 percent of the zero-tilt stagnation point heating rate. Data shown in figures 4 and 5 were used as the basis to calculate the hypothetical reentry heating rates for the CEV.

ALTERNATIVE MATERIAL CHOICES

Composite materials (for example, graphite/epoxy composites) have matured greatly in the 40 years since the design of the Apollo capsule, and have been widely applied to aerospace structures including the Space Shuttle orbiter. As shown in figure 6, the Space Shuttle orbiter cargo bay doors are fabricated with lightweight and high-strength composite sandwich panels. These curved composite panels are fabricated with NOMEX (E.I. duPont de Nemours and Company, Wilmington, Delaware) honeycomb core, which is an excellent insulator, and graphite/epoxy face sheets, which provide low heat conduction. The graphite/epoxy composite material has a weight density of $\rho = 0.05684$ lb/in^3 which is 56 percent of the weight density $\rho = 0.10130$ lb/in^3 of aluminum, and which provided great weight savings for the Space Shuttle orbiter.

The Space Shuttle orbiter graphite/epoxy composite cargo bay doors have exhibited excellent thermostructural performance; as such, graphite/epoxy composite sandwich construction could be an excellent candidate structural concept for the CEV reentry capsule wall structures.

The fact should also be kept in mind that the Space Shuttle orbiter graphite/epoxy composite cargo bay doors are in the shadow zone (wake) of the reentry heating, and are covered with flexible NOMEX Felt Reusable Surface Insulation (FRSI). This insulation has performed very well in protecting said composite cargo bay doors from overheating during STS flights (ref. 4). Since the conical aft-body of the CEV reentry capsule is in the leeward zone, in a position similar to that of the Space Shuttle orbiter cargo bay doors, NOMEX FRSI may also be a good candidate heat shield for the conical region of the CEV reentry capsule.

THE ABLATION PHENOMENON

The Apollo capsule used the ablative TPS material Avcoat 5026-39/HC-G, which has an ablation temperature of approximately 1200°F (ref. 3). Under extreme heat fluxes, this ablative TPS material can absorb large heat loads through phase change (charring) and shedding masses (ablation), reducing the heat load into the underlying TPS and substructures. Figure 7 shows the energy accommodation mechanisms of the ablative TPS material under discussion (ref. 5). The ablated TPS consists of a porous charred outer layer, a sublayer formed by pyrolysis (material decomposition by heat), and an inner virgin layer (fig. 7). The total applied heat load during the ablation period consists primarily of the following two major components:

1. The conduction heat load: for heating the virgin TPS and keeping it at the ablation temperature, T_A. The conduction heat load includes the heat losses through external and internal radiation, heat loss through internal convection, and conduction.
2. The ablation heat load: for outgassing, and for pyrolysis decomposition and charring of the TPS.

Table 2 lists the ablation properties of the Apollo TPS material, Avcoat 5026-39/HC-G (ref. 3).

Table 2. Ablative properties of Avcoat 5026-39/HC-G (the Apollo TPS material).

Combustion enthalpy	11,850 Btu/lb
Heat of vaporization	11,400 Btu/lb
Heat of decomposition	500 Btu/lb
Virgin density	1.9097×10^{-2} lb/in^3
Char density*	0.9549×10^{-2} lb/in^3

* The char density is approximately one-half of the virgin density.

As will be shown in the section "Virtual Ablation Analysis" below, the distribution of conduction and ablation heat loads can be estimated graphically using the results obtained from the nonablation thermal analysis.

HEAT–TRANSFER ANALYSIS

Heat-transfer analysis was performed using the Structural Performance and Resizing (SPAR) finite element thermal code (ref. 6). Two cases were analyzed. Case 1 was to conduct comparative studies of the heat-shielding characteristics of honeycomb sandwich panels fabricated with different materials. Case 2 was to study the performance of the TPS in protecting the CEV windward substructures during reentry heating (fig. 2).

The Unit–Cell Thermal Model

Figure 8 shows the honeycomb-core sandwich panel with core depth h_c = 0.5000 in., and two identical face sheets of thickness t_s = 0.0100 in. The honeycomb core is assumed to have right hexagonal cells with wall thickness t_c = 0.0015 in. Other dimensions are indicated in the inset of figure 8. The heat transfer across the sandwich panel may be reduced to the heat-transfer problems of a unit honeycomb cell.

Figures 9(a) and 9(b) show the thermal models (conduction and radiation) generated for the right hexagonal honeycomb unit cell (ref. 2). This unit-cell thermal model is to be used for studying the heat-shielding characteristics of honeycomb sandwich panel fabricated with different materials (ref. 2). Because this study is one of relative thermal performance (drops in temperature across the honeycomb-core depths), any arbitrary temperature loading may be used to heat the hot (lower) side of the panel. For the present analysis, the simple linearly-increasing temperature loading function presented in eq. (1) is used.

$$T(t) = 70 + 2.3t \tag{1}$$

where T is the temperature in degrees Fahrenheit, and t is time in seconds.

The cool (upper) side is unheated, however, the heat flow from the hot side to the cool side through conduction and internal radiation is allowed to radiate from the cool surface into a 70°F heat sink modeled with a radiation element [fig. 9(b)].

Two cases were considered for the cool surface radiation. In case 1, heat from the cool surface (point B) was allowed to radiate into an interior heat sinkset at a temperature of 70°F. In case 2, no radiation from the cool face sheet was allowed to radiate into an interior heat sink. The interior heat sink was modeled with a radiation element [fig. 9(b)] that was kept at constant temperature of 70°F to simulate the crew cabin wall temperature. The purpose of studying case 2 was to determine the amount by which structural temperatures will change if the interior radiation from the cool surface is neglected. The size of the unit-cell thermal model is listed in table 3.

Table 3. Size of unit-cell thermal model; right hexagonal cell.

Item	JLOC	K31	K41	R31	R41
Count	525	48	480	48	480

The Simple–Plug Thermal Model

Figure 10 shows the dimensions of the simple-plug thermal model generated for the generic CEV windward wall structures. This thermal model is to be used for studying the heat-shielding performance of the TPS in protecting the CEV windward wall substructures during reentry heating (fig. 2).

The generic CEV windward wall (fig. 2) has the dimensions shown in figure 10. The TPS-covered exterior wall is fabricated with graphite/epoxy composite face sheets and NOMEX honeycomb core. The interior aluminum sandwich wall (face sheets and honeycomb core) is made of 2219-T8XX aluminum (the same material as that used in the Space Shuttle orbiter structures). Both the interior and the exterior sandwich walls have the same core depth, h_c = 0.5000 in., and the same face sheet thickness, t_s = 0.010 in., and they are separated by a 2-in. gap (fig. 10). The TPS material is the ablative material Avcoat 5026-39/HC-G (ref. 3) used in the Apollo TPS; however, in the present thermal analysis the TPS ablation effect was not considered, and the TPS was modeled as a nonablating surface.

In the simple-plug thermal model (fig. 10), the TPS is modeled with 12 layers of eight-node brick elements (K81 conduction elements). Each of the face sheets and the honeycomb core of the exterior composite sandwich wall and the interior aluminum sandwich wall was modeled with a single K81 element. The internal and external radiation exchanges are modeled with four-node radiation elements (R41 elements). The interior sandwich wall was kept at 70°F to simulate a heat sink. The convection in the empty space is modeled with four-node convection elements (C41 elements) connecting the exterior and interior walls. All of the thermal properties used in the thermal model are listed in the appendix. The size of the simple-plug thermal model is listed in table 4.

Table 4. Size of simple-plug thermal model.

Item	JLOC	K41	K81	R41	C41
Count	84	1	18	4	6

Reentry Heating Rates

The Apollo 009 low Earth orbit reentry trajectory (altitude, velocity) (fig. 4, ref. 1) was used as the reentry trajectory for the CEV. The NASA Dryden aerodynamic heating program called TPATH (ref. 7) was used to calculate the reentry heating rates that were used in the CEV thermal analyses. From the sketch shown in figure 1, the CEV windward shallow spherical surface has an approximately 246.00 in. (6.25 m) radius. Based on this radius, two cases of the stagnation point heating rates were calculated:

1. The zero-tilt stagnation point heating rate ($\phi = 0°$).
2. The 1.4 amplification factor (1.4 × stagnation point heating rate) to simulate the heating rate at the stagnation point which has migrated toward the upper toroidal shoulder when the CEV is at $\phi = 18°$ angle of tilt [based on Apollo wind tunnel data (ref. 1)].

When making the stagnation heating calculations, the surface temperature was limited to 1200°F. Limiting the surface temperature to 1200°F results in a conservative estimate of the heating rates because the actual surface temperature may exceed 1200°F. The reason for this is that the stagnation heating rates are a direct function of the difference between the stagnation temperature, T_t and the surface temperature T_s, $(T_t - T_s)$. Therefore, any increase in the surface temperature, above the 1200°F limit imposed for these calculations, will result in a decrease in the value of $(T_t - T_s)$ and consequently lower heating rates.

Figure 11 shows the time history of the 1.0 and 1.4 amplified stagnation point heating rates calculated from the TPATH program using the Apollo low Earth orbit reentry trajectories shown in figure 4. The time $t = 0$ s in the plots is defined as the reentry time. Note from figure 11 that the high-heating regions of those surface heating curves are steeple-shaped with pointed peaks, and are entirely different from the Space Shuttle orbiter surface heating curves, for which the high-heating region of a typical reentry heating curve was plateau-shaped and lasted over approximately 600 s (ref. 4).

STRUCTURAL TEMPERATURES

The structural temperatures calculated for the honeycomb sandwich panel and the generic CEV windward wall structures are presented below.

The Unit Honeycomb Cell

Figure 12 shows the temperature-time histories at the hot side (point A) and the cool side (point B) of the honeycomb sandwich panel. The temperature curve for point A was calculated from eq. (1), and is a straight line starting from 70°F at time $t = 0$ s and ending at 300°F at time $t = 100$ s. The SPAR-calculated temperature curves for point B at the cool side of the aluminum sandwich panel and of the graphite/epoxy sandwich panel are shown for two interior radiation cases: 1) considering radiation from the cool face sheet into a 70°F interior heat sink, and 2) considering no radiation from the cool face sheet into an interior heat sink. The aluminum honeycomb sandwich core shows very poor heat-shielding performance with small temperature drops $\Delta T = \{18, 11\}$°F (at $t = 100$ s) from point A to point B for the case with and the case without interior radiation. The heat-shielding performance of the sandwich core is the amount of temperature drop between the hot side (point A) and the cool side (point B) that the sandwich core can provide. The difference in temperature drops, ΔT, between the case with interior radiation and the case without interior radiation is 7°F (at $t = 100$ s).

On the other hand, the composite honeycomb core shows excellent heat-shielding performance with temperature drops $\Delta T = \{148, 126\}$°F (at $t = 100$ s) from point A to point B for the case with and the case without interior radiation. The difference in temperature drops ΔT between these two cases of interior radiation is 22°F (at $t = 100$ s) (approximately three times larger). Table 5 summarizes the temperatures at the cool face sheet T (point B) of the sandwich panel at $t = 100$ s [when T (point A) = 300°F].

Table 5. Temperatures at cool face sheet (point B) of sandwich panels at $t = 100$ s; T (point A) = 300°F (temperature limit of graphite/epoxy composite).

	Aluminum		Graphite/epoxy	
	T (point B), °F	ΔT ,°F	T (point B), °F	ΔT ,°F
With interior radiation	282	18	152	148
Without interior radiation	289	11	174	126
Decrease in ΔT		7		22

Table 5 clearly shows that graphite/epoxy sandwich panel outperforms aluminum sandwich panel under the same geometrical dimensions because of the lower thermal conductivity and lower material density of the graphite/epoxy sandwich panel.

The Crew Exploration Vehicle Windward Wall

Figure 13 shows the SPAR-calculated TPS surface temperature and the substructural composite sandwich temperatures plotted as functions of time based on the 1.0 × stagnation point heating rates. The TPS surface temperature reached a maximum of 3077°F at 65 s from reentry. The duration of time that the TPS was heated above the ablation temperature of 1200°F was 113 s (from t = 37 s to t = 150 s). The temperatures of the composite sandwich interior face sheet for the three different cases of TPS thickness h = {2.8, 1.5, 1.0} in. reached values of T = {70, 88, 235}°F at touchdown. The composite sandwich temperatures will continue to increase after the CEV land touchdown. In the case of a water touchdown, the cooling effect starts immediately and, therefore, the values of T = {70, 88, 235}°F will be the true maximum temperatures at splashdown for the composite sandwich panel.

Figure 14 shows the SPAR-calculated TPS surface temperature and the underneath composite sandwich temperatures plotted as a function of time based on the 1.4 × stagnation point heating rates. The TPS surface temperature reached a maximum 3379°F at 65 s from reentry. The duration of time that the TPS was overheated above the ablation temperature of 1200°F was 137 s (from t = 33 s to t = 170 s). The composite sandwich temperatures for the different TPS thicknesses of h = {2.8, 1.5, 1.0} in. reached their respective values of T = {70, 89, 259}°F at touchdown.

Figure 15 shows temperature distributions across the CEV windward wall at different time steps for the TPS thickness of h = 2.8 in. (the Apollo TPS). Notice that the composite sandwich substructure is practically unheated because the TPS is sufficiently thick. At 65 s (peak heating), the surface layers heated above 1200°F are graphically estimated from figure 15 as {0.18, 0.19} in. depth, respectively, for the 1.0 × and 1.4 × applied stagnation point heating rate analysis. At t = 220 s and t = 380 s (6 s after touchdown time t = 374 s) the TPS surface temperature became lower than the maximum temperatures at the interior of the TPS because the TPS surface experiences convective and radiation cooling during the latter part of the flight trajectory. Table 6 summarizes the key data presented in the section "The Crew Exploration Vehicle Windward Wall" above.

Table 6. Overheated TPS layer thicknesses and overheated durations.

Heating	Overheated layer thickness, in.	Overheated duration, s
$1.0\,\dot{q}_{\mathrm{Stag}}$	0.18	113
$1.4\,\dot{q}_{\mathrm{Stag}}$	0.19	137

Figure 16 shows the plots of composite sandwich (TPS-side face sheet) maximum temperatures as functions of TPS thickness h for the two cases of heating. Note that the differences between the substructural temperatures associated with the two heating cases did not appear until the TPS thickness h was reduced from h = 2.8 in. to nearly h = 1.6 in.; the differences then started to magnify as the TPS thickness became less than 1.6 in. Note also that the composite maximum

temperatures reached the limit temperature of 300°F when the thickness of the TPS was reduced to $h = \{0.900, 0.937\}$ in., respectively, for the 1.0 × and 1.4 × stagnation point heating rates. Table 7 lists the composite sandwich temperature data used in plotting figure 16.

Table 7. Composite sandwich wall maximum temperatures, T_{SW} .

TPS h, in.	T_{SW} ($\dot{q}_{Stag}$),°F (1)	T_{SW} ($1.4\,\dot{q}_{Stag}$),°F (2)	Difference, °F (2) – (1)
2.8 (Apollo)	70	70	0
2.0	71	71	0
1.8	74	74	0
1.6	81	83	2
1.5	88	92	4
1.4	100	105	5
1.2	145	155	10
1.1	182	196	14
1.0	232	255	23
0.937	273	300*	27
0.9	300*	329	29
0.8	382	422	40
0.7	473	540	67

* Limit temperature for composite substructures.

WEIGHT OF THE THERMAL PROTECTION SYSTEM

The weight, W, of the windward TPS may be calculated from eq. (2)

$$W = \rho h(2\pi r_c c) \tag{2}$$

where r_c is the radius of the CEV forebody spherical shell, and c is the height of the spherical segment. For the following numerical input values for the generic CEV case:

$\rho = 1.9097 \times 10^{-2}$ lb/in^3 (the Apollo TPS material)
$h = 1.4$ in.
$r_c = 246$ in. (≈ 6.25 m)
$c = 21$ in.

the CEV windward TPS weight, W, can be calculated from eq. (3) shown below.

$$W = (1.9097 \times 10^{-2})(1.4)(2\pi \times 246 \times 21) \approx 868 \text{ (lb)} \tag{3}$$

VIRTUAL ABLATION ANALYSIS

In the preliminary thermal analyses discussed above, the thermal properties of the virgin ablative Apollo TPS material were used. No ablation effect of the TPS (that is, no heat of vaporization) was included in the analysis. Nevertheless, the results of the previous nonablating heat-transfer analysis may be used to arrive at an estimation of the ablation heat load and the TPS recession layer thickness. A graphical method (virtual ablation analysis) was developed to estimate these values.

To illustrate the graphical determination of the heat-load distribution during the applied ablation period, both the 1.0 × stagnation point heating case (case 1) and the 1.4 × stagnation point heating case (case 2) were considered.

The area under each heating rate curve in figure 11 was used to determine the total heat load applied to the CEV thermal model. To help determine the portion of the heat load not directed toward the ablation process, results from figures 13 and 14 were used to find the possible bounds of when the ablation process would occur. Keep in mind that the heating rate area below 1200°F (fig. 13 or fig. 14) does not contribute directly to the ablation process, and could be ignored in the graphical ablation analysis. For easy visualization of the graphical method, the heating curves (fig. 11) and the corresponding TPS surface temperature curve (fig. 13 or fig. 14) were plotted together in figures 17 and 18, respectively, for case 1 and case 2.

Figure 17 shows that for case 1 (1.0 × stagnation point heating), the TPS surface temperature exceeded the ablative temperature T_A = 1200°F between t = 37 s and t = 150 s. Figure 18 shows that for case 2 (1.4 × stagnation point heating), the TPS surface temperature exceeded T_A = 1200°F between t = 33 s and t = 170 s. It is clear that ablation could take place within those overheated time periods. The times t = 37 s (for case 1) and t = 33 s (for case 2) are the ablation initiation times, but as will be seen in the following section, "Types of Heat Loads," the times t = 150 s (for case 1) and t = 170 s (for case 2) may not necessarily be the ablation termination times because the TPS, overheated above T_A = 1200°F after t = 37 s (for case 1), and t = 33 s (for case 2) was assumed intact and, therefore, required more time to cool down to T_A = 1200°F at t = 150 s (for case 1) or t = 170 s (for case 2) as compared with the ablated case. In the actual ablation case, as the TPS surface layer is heated above 1200°F, ablation will occur and the TPS thickness will be reduced; therefore, the ablation period could be slightly shorter. As will be seen in the next section, "Types of Heat Loads," the virtual ablation ended slightly earlier than t = 150 s (for case 1) or t = 170 s (for case 2).

Types of Heat Loads

During the first 37 s (case 1, fig. 17) or the first 33 s (case 2, fig. 18) of the heating cycle, the total heat load is used to heat the virgin TPS surface to 1200°F. Once the TPS has reached 1200°F, part of the heat load is required to maintain this temperature during the ablation period. This portion of the heat load consists of the heat conducted into the TPS and substructure, the heat capacity of the TPS and substructures, the heat radiated away from the surface of the TPS, and the heat loss to the interior heat sink (crew cabin) by internal radiation and convection. In the present

analysis, this portion of the heat load is called the conduction heat load, q_C (Btu/in^2). The remaining heat load during the time the surface temperature is above 1200°F can be used in the ablation of the TPS and is called the ablation heat load, q_A (Btu/in^2). The total heat load, q_T (Btu/in^2), during the ablation period then consists of the sum of the conduction heat load, q_C, and the ablation heat load, q_A, as shown in eq. (4) below.

$$q_T = q_C + q_A \tag{4}$$

Determinations of Heat Loads

Before determining the heat loads, one must first determine the conduction heating rate, $\dot{q}_C$, the ablation starting time, t_1, and the ablation ending time, t_2. The 1.0 × stagnation point heating rate reentry heating case will be used to illustrate the determination of the different heat loads during the ablation period.

As shown in figure 17, the initial heat load (the area under the heating curve portion 0A) was used to heat the TPS surface to 1200°F at t = 37 s. After t = 37 s the TPS surface temperature will continue to rise and will exceed 1200°F assuming the TPS is nonablative (fig. 17). Therefore, the time step $t = t_1$ = 37 s is to be considered the ablation starting time, however, the ablation ending time, t_2, is not yet known and could be determined as described in the following three paragraphs.

After t_1 = 37 s, one must first determine the portion of the conduction heat load that is not directed toward the ablation process. This conduction heat load, q_C (Btu/in^2), is to be used to continue heating the TPS and to maintain the TPS surface temperature at 1200°F throughout the ablation period. The remaining heat load, q_A (Btu/in^2), is to be used to ablate the TPS. As shown in figure 17, the conduction heating curve is the horizontal line BC with constant heating rate $\dot{q}_C$ (Btu/in^2-s), starting from point B (t_1 = 37 s) and ending at point C on the original reentry heating curve. The time step at point C should be considered as the ablation ending time t_2 which is yet to be determined. Beyond point C, the ablation process should end because the reentry heating rate is now less than the conduction heating rate $\dot{q}_C$ (there is no more excess heat energy for ablation).

To find the value of $\dot{q}_C$ (for the BC region) that would maintain the TPS surface temperatures at 1200°F over the ablation period, repeated finite-element heat-transfer analyses were carried out using different trial input values of $\dot{q}_C$ to the thermal model and examining the output TPS surface temperatures. The correct value of $\dot{q}_C$ was found to be $\dot{q}_C$ = 0.032 Btu/in^2-s for the Avcoat 5026-39/HC-G (the Apollo TPS material). The TPS surface temperatures calculated using the correct conduction heating rate ($\dot{q}_C$ = 0.032 Btu/in^2-s) are plotted in figures 17 and 18 with solid symbols connected with broken curve. The data points practically fell on the 1200°F temperature line over the BC region.

Once the correct value of $\dot{q}_C$ (the height of the conduction heating curve BC) is determined, the ablation ending time, t_2, can be found. The reentry heating data points do not include an

exact data point matching the height of BC ($\dot{q}_C$ =0.032 Btu/in^2-s). Therefore, three points curvilinear interpolation was used to locate point C with the value of $\dot{q}(t_2) = \dot{q}_C$ = 0.032 Btu/in^2-s (the height of the BC curve). The time step for point C thus determined produced an ablation ending time of t_2 = 124 s. The time durations $t_1 - t_2$ = 87 s (= 124 – 37) s may then be defined as the virtual ablation period.

Figure 18 shows a similar plot for graphical virtual ablation analysis for the 1.4 × stagnation point heating rate case. Because of the higher heating rate, the ablation period started slightly earlier at t_1 = 33 s and ended slightly later at t_2 = 140 s with an ablation duration of $t_1 - t_2$ = 107 s (= 140 – 33) s. Table 8 summarizes the results of the graphically-determined ablation period data for the different heating cases.

Table 8. Graphically-determined virtual ablation data.

Heating	Ablation starting time, sec	Ablation ending time, s	Ablation period, s
$1.0\,\dot{q}_{\text{Stag}}$	37	124	87
$1.4\,\dot{q}_{\text{Stag}}$	33	140	107

Once the ablation starting and ending times $\{t_1,\ t_2\}$ and the conduction heating rate, $\dot{q}_C$, are determined, the three heat loads $\{q_T, q_C, q_A\}$ during the ablation period, $t_1 \le t \le t_2$, may be obtained by integrating the proper heating rate over the ablation time interval, as shown in eqs. (5) – (7) below.

The total heat load: the integration of the reentry heating rate, $\dot{q}(t)$, over $t_1 \le t \le t_2$:

$$q_T = \int_{t_1}^{t_2} \dot{q}(t)dt \tag{5}$$

= the area under the reentry heating curve bounded by t_1 and t_2 .

The conduction heat load: the integration of the conduction heating rate, $\dot{q}_C$, (constant) over $t_1 \le t \le t_2$:

$$q_C = \int_{t_1}^{t_2} \dot{q}_C dt = \dot{q}_C(t_2 - t_1) \tag{6}$$

= the area under the conduction heating curve BC bounded by t_1 and t_2 .

The ablation heat load: integration of $[\dot{q}(t) - \dot{q}_C]$ over $t_1 \le t \le t_2$:

$$q_A = q_T - q_C = \int_{t_1}^{t_2} [\dot{q}(t) - \dot{q}_C] dt \quad ; \quad \dot{q}_C = \text{constant} \tag{7}$$

= the area between the reentry heating curve and the conduction heating curve BC bounded by t_1 and t_2.

The values of the three heat loads $\{q_T, q_C, q_A\}$ calculated from eqs. (5) – (7) are summarized in table 9 for the different cases of reentry heating rates.

Table 9. Heat-load distributions for ablation periods.

Heating	q_T, Btu/in^2	q_C, Btu/in^2	q_A, Btu/in^2
$1.0\,\dot{q}_{\text{Stag}}$	19.89	2.78	17.10
	(100%)	(14%)	(86%)
$1.4\,\dot{q}_{\text{Stag}}$	28.77	3.42	25.35
	(100%)	(12%)	(88%)

( ) = percent of total heat load q_T.

Note that for ablative TPS material, only small portions (12 to 14 percent) of the total heat loads will penetrate into the intact TPS, and the majority of the heat loads (86 to 88 percent) are removed through ablation.

Thermal Protection System Recession Thicknesses

The heat of vaporization (including charring), q_V, of the Apollo TPS material is listed as q_V = 11,900 Btu/lb (ref. 3). Using the virgin density $\rho = 1.9097 \times 10^{-2}$ lb/in^3 of the Apollo TPS material, the Btu/lb unit of q_V may be converted to Btu/in^3 as $q_V = 11{,}900 \times 1.9097 \times 10^{-2} = 227.25$ lb/in^3. The TPS recession layer thickness, δ, may be calculated from eq. (8) as

$$\delta = \frac{q_A}{q_V} = \frac{q_A}{227.25} \text{ (in.)} \tag{8}$$

and the weight, ΔW, of the vaporized TPS layer may be calculated from eq. (9) as

$$\Delta W = \frac{\delta}{h} W = \frac{\delta}{1.4} \times 868 \text{ (lb)} \tag{9}$$

where h = 1.4 in. [eq. (2)] is used as the original intact TPS thickness. Table 10 lists the calculated values of the TPS recession layer thicknesses, δ, and the ablated weights, ΔW.

Table 10. Ablated TPS layer thicknesses, δ, and ablated weights, ΔW; h = 1.4 in., W = 868 lb.

Heating	δ, in.	ΔW, lb	$\frac{\delta}{h}\left(=\frac{\Delta W}{W}\right)\times 100\%$
$1.0\,\dot{q}_{\text{Stag}}$	0.08	49.60	5.71%
$1.4\,\dot{q}_{\text{Stag}}$	0.11	68.20	7.86%

Those TPS recession layer thicknesses, δ, (table 10) are insignificant compared with the initial intact TPS thickness h. It was shown earlier in figure 16 that even if the TPS thickness is reduced to h = 1.4 in. (one-half of the original TPS thickness of h = 2.8 in.) the substructural temperature level is hardly affected.

Ignoring the heat removed by the ablation process and retaining the overheated TPS material in the present thermal model is self-compensating in the calculated results. Therefore, the present results are reasonably good as a first approximation.

Temperature Distributions

As discussed earlier, during the virtual ablation period the conduction heating rate $\dot{q}_C$ = 0.032 (Btu/in^2-s) was used to maintain the TPS surface temperature at 1200°F over the virtual ablation period. The heating rates along the conductive heating curves 0ABCD (figs. 17 and 18) were then used to recalculate the structural temperatures for the 1.0 × and 1.4 × stagnation point heating rates.

Figures 19(a) and 19(b) show the structural temperature distributions across the CEV wall at different time steps for two TPS thicknesses h = {2.8, 1.4} in. Notice that unlike in the nonablation cases (figs. 15 and 16), under virtual ablation the TPS surface temperatures never exceeded 1200°F. The TPS temperature curves [figs. 19(a) and 19(b)] for the two heating cases are practically indistinguishable until touchdown. By reducing the TPS thickness from h = 2.8 in. [fig. 19(a)] to h = 1.4 in. [fig. 19(b)], the TPS-side composite sandwich temperature increased from 70°F [fig. 19(a)] to 85°F [fig. 19(b)] (an insignificant increase of 15°F) for the two cases of stagnation point heating rates.

Figures 20 and 21 show, respectively, the structural temperature distributions across the CEV wall at different time steps for TPS thicknesses h = {1.32, 1.29} in. (assumed constant during flight). The TPS thicknesses h = {1.32, 1.29} in. are to simulate the virtual ablation by removing the recession thicknesses δ = {0.08, 0.11} in. (table 10) from h = 1.4 in. [fig. 19(b)] respectively for the 1.0 × and 1.4 × stagnation point heating rates. Notice that when the TPS thickness was eroded from h = 1.4 in. to h = {1.32, 1.29} in. respectively for the 1.0 × and 1.4 × stagnation point heating rate cases, the TPS-side composite sandwich temperatures increased from 85°F [fig. 19(b)] to 92°F (fig. 20) and 96°F (fig. 21) respectively (insignificant increases of {7, 11}°F).

Figures 22 and 23 show, respectively, the TPS-side composite face sheet maximum temperatures (at touchdown) plotted as functions of the TPS thickness h for the 1.0 × and 1.4 × stagnation point heating rate cases with virtual ablation. The composite temperature curves for nonablation cases (taken from figure 16) are also shown for comparison. Notice that the effect of virtual ablation started to appear when h became less than $h = 2.0$ in. Notice also that with virtual ablation, the substructural composite temperatures reached the limit of 300°F at TPS thicknesses $h = \{0.717, 0.733\}$ in., which are the reductions of {0.183, 0.204} in. from $h = \{0.900, 0.937\}$ in. of the nonablation cases because of lower TPS surface temperatures. The TPS thicknesses of $h = \{0.717, 0.733\}$ in. may then be considered to be the allowable minimum for the CEV zero-tilt and 18-deg tilt stagnation point TPS thicknesses for the low Earth orbit reentry trajectory. The composite temperature data for plotting figures 22 and 23 are listed, respectively, in tables 11 and 12.

Table 11. Composite sandwich wall maximum temperatures, T_{SW} , at touchdown; 1.0 × stagnation point heating rate; with and without virtual ablation.

h, in. (TPS)	T_{SW} ,°F (no ablation) (1)	T_{SW} ,°F (virtual ablation) (2)	Temperature reduction, °F (1) – (2)
2.8 (Apollo)	70	70	0
2.0	71	71	0
1.8	74	72	2
1.6	81	75	6
1.5	88	79	9
1.4	100	85	15
1.32	114	92	22
1.2	145	108	37
1.1	182	129	53
1.0	232	158	74
0.9	300*	198	102
0.8	382	249	133
0.717	457	300*	157
0.7	473	312	161

* The limit temperature for composite substructures.

Table 12. Composite sandwich wall maximum temperatures, T_{SW} , at touchdown; 1.4 × stagnation point heating rate; with and without virtual ablation.

h, in. (TPS)	T_{SW} ,°F (no ablation) (1)	T_{SW} ,°F (virtual ablation) (2)	Temperature reduction, °F (1) – (2)
2.8 (Apollo)	70	70	0
2.0	71	71	0
1.8	74	72	2
1.6	83	75	8
1.5	92	79	13
1.4	105	85	20
1.29	128	96	32
1.2	155	110	45
1.1	196	131	65
1.0	255	161	94
0.937	300*	186	114
0.9	329	203	126
0.8	422	257	165
0.733	502	300*	202
0.7	540	323	217

* The limit temperature for composite substructures.

Note from tables 11 and 12 that the effect of ablation on the substructural temperature reduction is negligible when the TPS is relatively thick, but gradually becomes significant as the TPS thickness is reduced.

SUMMARY

The following three sections summarize the results of the heat-shielding performance analysis of honeycomb sandwich panels, and the hypothetical reentry heat-transfer analysis (nonablative and virtual ablative) of generic crew exploration vehicle reentry capsule windward wall structures using Apollo low Earth orbit reentry trajectories.

Heat–Shielding Analysis Results

1. The contribution of internal radiation to the sandwich core-wise temperature drop is very small for the aluminum sandwich panel, but is significant for the graphite/epoxy sandwich panel as heating continues.
2. The aluminum sandwich panel has extremely poor heat-shielding properties because of high conductivity.

3. The graphite/epoxy sandwich panel thermostructurally outperforms the aluminum sandwich panel under the same geometry because of superior heat-shielding qualities and a lower material density.

Nonablation Analysis Results

1. With a nonablating TPS, the windward thermal protection system surface temperatures reached maximum values of {3077, 3379}°F at $t = 65$ s, respectively, for the 1.0 × and 1.4 × stagnation point heating rates.
2. For the thermal protection system thicknesses $h = \{2.8, 1.5, 1.0\}$ in., the associated substructural composite sandwich temperatures reached {70, 88, 235}°F and {70, 89, 259}°F at touchdown, respectively, for the 1.0 × and 1.4 × stagnation point heating rates.
3. When the thermal protection system thicknesses are reduced to $h = \{0.900, 0.937\}$ in., respectively, for the 1.0 × and 1.4 × stagnation point heating rates, the substructural composite sandwich temperature will reach the limit temperature of 300°F. Therefore, $h = \{0.900, 0.937\}$ in. may be considered to be the allowable minimum thermal protection system thicknesses, respectively, for the two heating cases.
4. For a thermal protection system thickness of 1.4 in., the proposed crew exploration vehicle windward thermal protection system weight is approximately 868 lb.

Virtual Ablation Analysis Results

1. The results of the nonablative analysis were used to develop the graphical virtual ablation approximation method to determine the period of time during which ablation would occur. By estimating the area under the heating rate curve bounded by the ablation time period, the amount of energy that can be attributed to ablating the TPS (the ablative heat load) can be determined; thus, the TPS recession thicknesses can be calculated.
2. For the 1.0 × and 1.4 × stagnation point heating rates, analysis indicated that during the time history when the TPS surface was heated above 1200°F, {86, 88}% of the total heat load can be used for the ablation process, and the remaining {14, 12}% for maintaining the virgin TPS surface temperature at 1200°F during ablation periods.
3. For the 1.0 × stagnation point heating rate analysis, the virtual ablation period lasted for 87 s (from $t = 37$ s to $t = 124$ s).
4. For the 1.4 × stagnation point heating rate analysis, the virtual ablation period lasted for 107 s (from $t = 33$ s to $t = 140$ s).
5. Based on the virtual ablation approximation method, the TPS recession thicknesses of {0.08, 0.11} in. were calculated, respectively, for the cases of 1.0 × and 1.4 × stagnation point heating rates, and are insignificant when compared with the intact TPS thickness.

6. For the zero-tilt (1.0 × stagnation point heating rate) and 18-degree-tilt (1.4 × stagnation point heating rate) stagnation points, TPS thicknesses of h = {0.717, 0.733} in. are adequate to keep the substructural composite sandwich temperature below the limit of 300°F. Therefore, h = {0.717, 0.733} in. may be considered to be the allowable minimum stagnation point TPS thicknesses, respectively, for the zero-tilt and 18-degree tilt of the generic crew exploration vehicle.

Dryden Flight Research Center
National Aeronautics and Space Administration
Edwards, California 93523
June 27, 2005

APPENDIX
THERMAL PROPERTIES OF CANDIDATE MATERIALS

Radiation Properties

Radiation properties used for the space element (heat sinks) are listed in table A1.

Table A1. Radiation properties of the space element (heat sinks).

T, °R	ε	a	r
460	1	1	0

The 460°R used in table A1 is the average temperature of the atmosphere during the high-heating portion of the reentry flight (from an altitude of 260,000 ft msl to an altitude of 150,000 ft msl).

The radiation properties used for internal radiation exchanges are shown in table A2.

Table A2. Radiation properties for internal radiation exchanges.

T, °R	ε	a	r
530	0.667	0.667	0.333

Thermal Properties

Materials thermal properties are presented in tables A3–A7. Shown are the thermal properties of 2219-T8XX aluminum, aluminum sandwich core, graphite/epoxy composite face sheets, NOMEX sandwich core, and Avcoat 5026-39/HC-G.

Table A3. Thermal properties of 2219-T8XX aluminum (used in the Space Shuttle orbiter structure).

T, °R	ρ, lb/in^3	c_p, Btu/lb-°F	k_1, Btu/in-s-°F	k_2, Btu/in-s-°F	k_3, Btu/in-s-°F
360	0.1013	0.183	1.4800-3	1.4800-3	1.4800-3
460	0.1013	0.195	1.5972-3	1.5972-3	1.5972-3
560	0.1013	0.206	1.7130-3	1.7130-3	1.7130-3
660	0.1013	0.215	1.8056-3	1.8056-3	1.8056-3
760	0.1013	0.222	1.8981-3	1.8981-3	1.8981-3
860	0.1013	0.228	1.9606-3	1.9606-3	1.9606-3
960	0.1013	0.234	2.0139-3	2.0139-3	2.0139-3
1060	0.1013	0.250	2.0694-3	2.0694-3	2.0694-3

Table A4. Thermal properties of aluminum sandwich core.

T, °R	ρ, lb/in^3	c_p, Btu/lb-°F	k_1, Btu/in-s-°F	k_2, Btu/in-s-°F	k_3, Btu/in-s-°F
360	1.664-3	0.213	2.0076-5	2.0076-5	2.3900-5
460	1.664-3	0.214	2.1695-5	2.1695-5	2.5827-5
560	1.664-3	0.215	2.3287-5	2.3287-5	2.7723-5
660	1.664-3	0.217	2.4542-5	2.4542-5	2.9217-5
760	1.664-3	0.218	2.5843-5	2.5843-5	3.0765-5
860	1.664-3	0.220	2.6715-5	2.6715-5	3.1804-5
960	1.664-3	0.222	2.7464-5	2.7464-5	3.2695-5
1060	1.664-3	0.225	2.8242-5	2.8242-5	3.3622-5

Table A5. Thermal properties of graphite/epoxy composite face sheets (used in the Space Shuttle orbiter cargo bay doors).

T, °R	ρ, lb/in^3	c_p, Btu/lb-°F	k_L, Btu/in-s-°F	k_T, Btu/in-s-°F	$k_3 (= k_T)$, Btu/in-s-°F
160	5.6944-2	0.049	1.2269-5	0.3287-5	0.3287-5
170	5.6944-2	0.053	1.3426-5	0.3472-5	0.3472-5
310	5.6944-2	0.112	2.7546-5	0.5324-5	0.5324-5
360	5.6944-2	0.132	3.1481-5	0.5903-5	0.5903-5
410	5.6944-2	0.152	3.4954-5	0.6481-5	0.6481-5
560	5.6944-2	0.208	4.5370-5	0.8333-5	0.8333-5
660	5.6944-2	0.242	4.9537-5	0.9028-5	0.9028-5
760	5.6944-2	0.277	5.3009-5	0.9954-5	0.9954-5
860	5.6944-2	0.308	5.6019-5	1.0880-5	1.0880-5
960	5.6944-2	0.340	5.8796-5	1.1667-5	1.1667-5
1060	5.6944-2	0.379	6.1574-5	1.2454-5	1.2454-5

Table A6. Thermal properties of NOMEX sandwich core (used in the Space Shuttle orbiter cargo bay doors).

T, °R	ρ, lb/in^3	c_p, Btu/lb-°F	k_1, Btu/in-s-°F	k_2, Btu/in-s-°F	k_3, Btu/in-s-°F
530	1.7361-3	0.38	0.8588-6	0.8588-6	1.0224-6

Table A7. Thermal properties of Avcoat 5026-39/HC-G (the Apollo TPS material).

T, °R	ρ, lb/in^3	c_p, Btu/lb-°F	k_1, Btu/in-s-°F	k_2, Btu/in-s-°F	k_3, Btu/in-s-°F
360	1.9097-2	0.385	0.3241-5	0.3241-5	0.3241-5
460	1.9097-2	0.385	0.3241-5	0.3241-5	0.3241-5
660	1.9097-2	0.440	0.3241-5	0.3241-5	0.3241-5
960	1.9097-2	0.520	0.3241-5	0.3241-5	0.3241-5
1160	1.9097-2	0.575	0.3241-5	0.3241-5	0.3241-5
1360	1.9097-2	0.655	0.3241-5	0.3241-5	0.3241-5
1460	1.9097-2	0.655	0.3241-5	0.3241-5	0.3241-5
1660	1.9097-2	0.655	0.3241-5	0.3241-5	0.3241-5
charring starts (ρ, k_1,k_2,k_3 change in values)					
1860	0.9549-2*	0.655	0.5093-5	0.5093-5	0.5093-5
2260	0.9549-2*	0.655	0.8218-5	0.8218-5	0.8218-5
2460	0.9549-2*	0.655	0.9838-5	0.9838-5	0.9838-5
2860	0.9549-2*	0.655	1.2500-5	1.2500-5	1.2500-5
3060	0.9549-2*	0.655	1.3773-5	1.3773-5	1.3773-5
3460	0.9549-2*	0.655	1.6204-5	1.6204-5	1.6204-5

* The char density is approximately one-half of the virgin density.

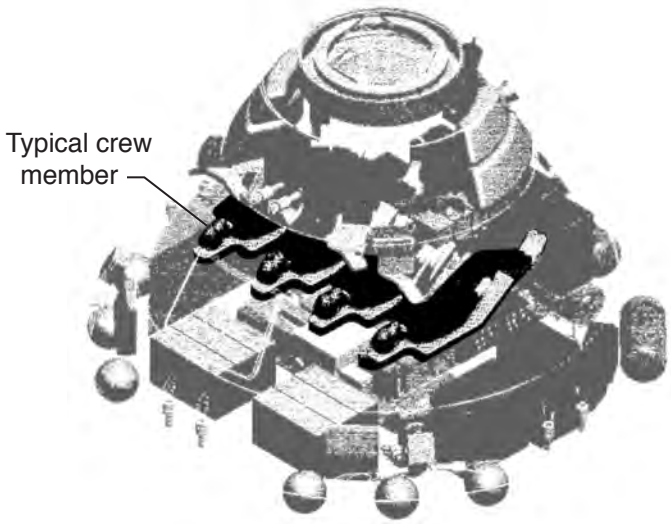

Figure 1(a). Interior view.

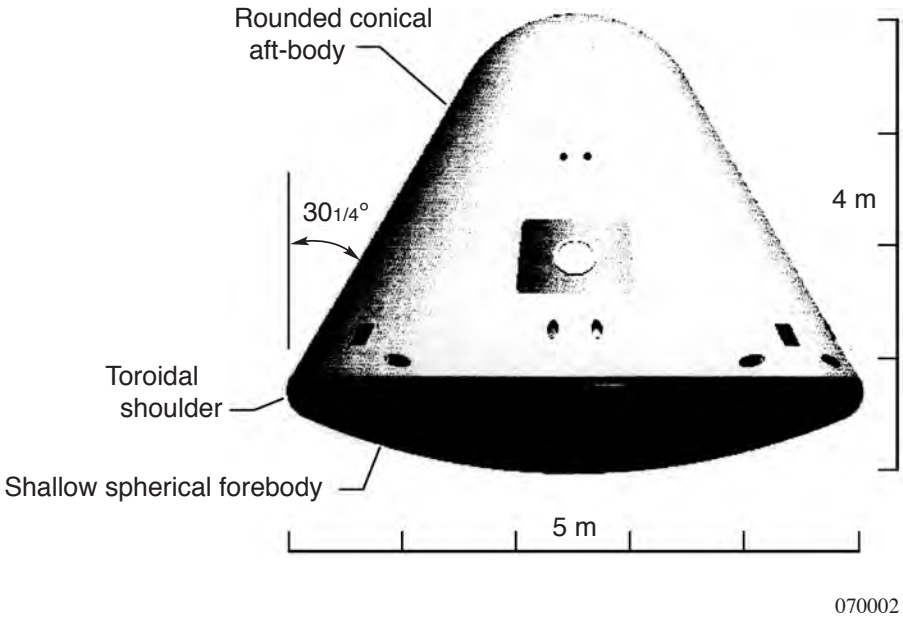

Figure 1(b). Exterior view.

Figure 1. Geometry of a candidate CEV (crew exploration vehicle).

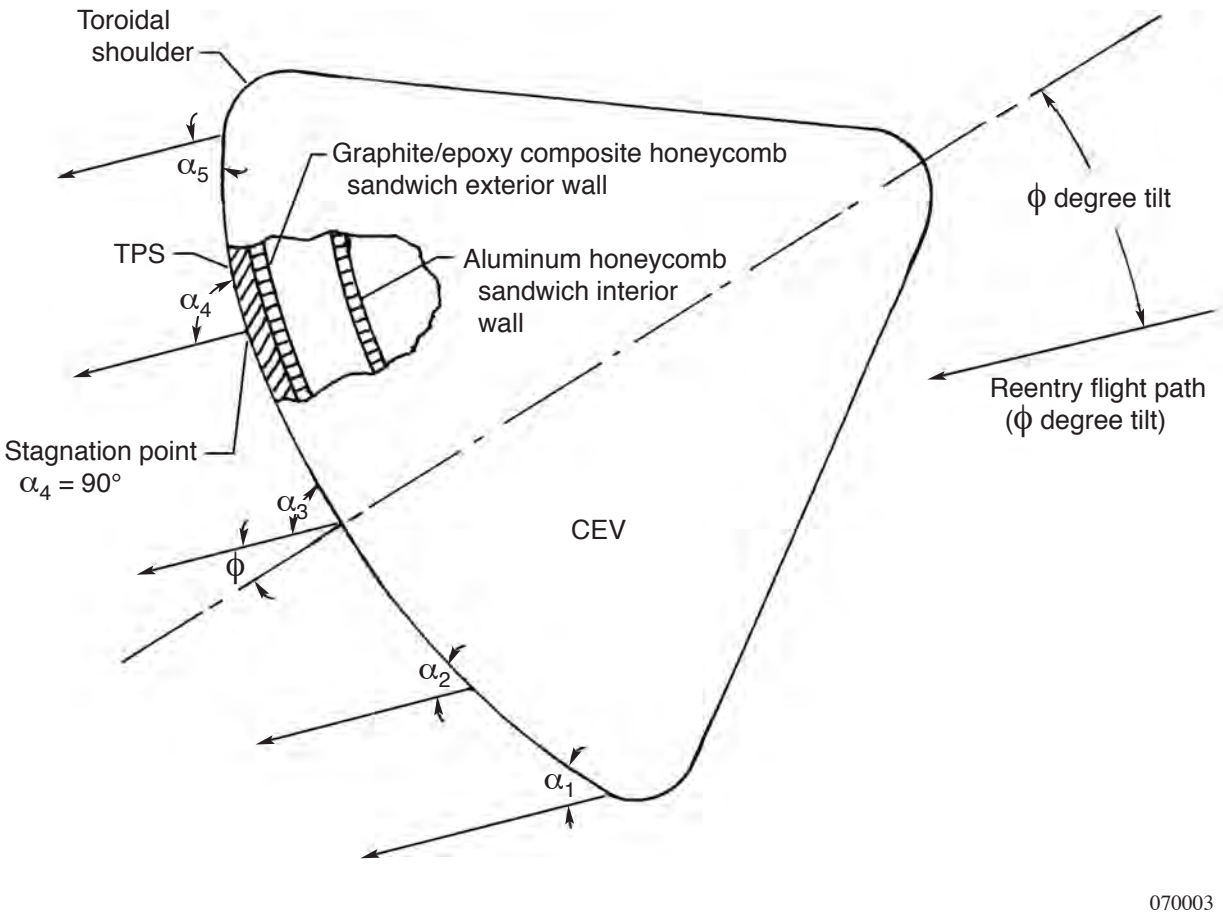

Figure 2. The CEV reentry flight at ϕ-degree angle of tilt.

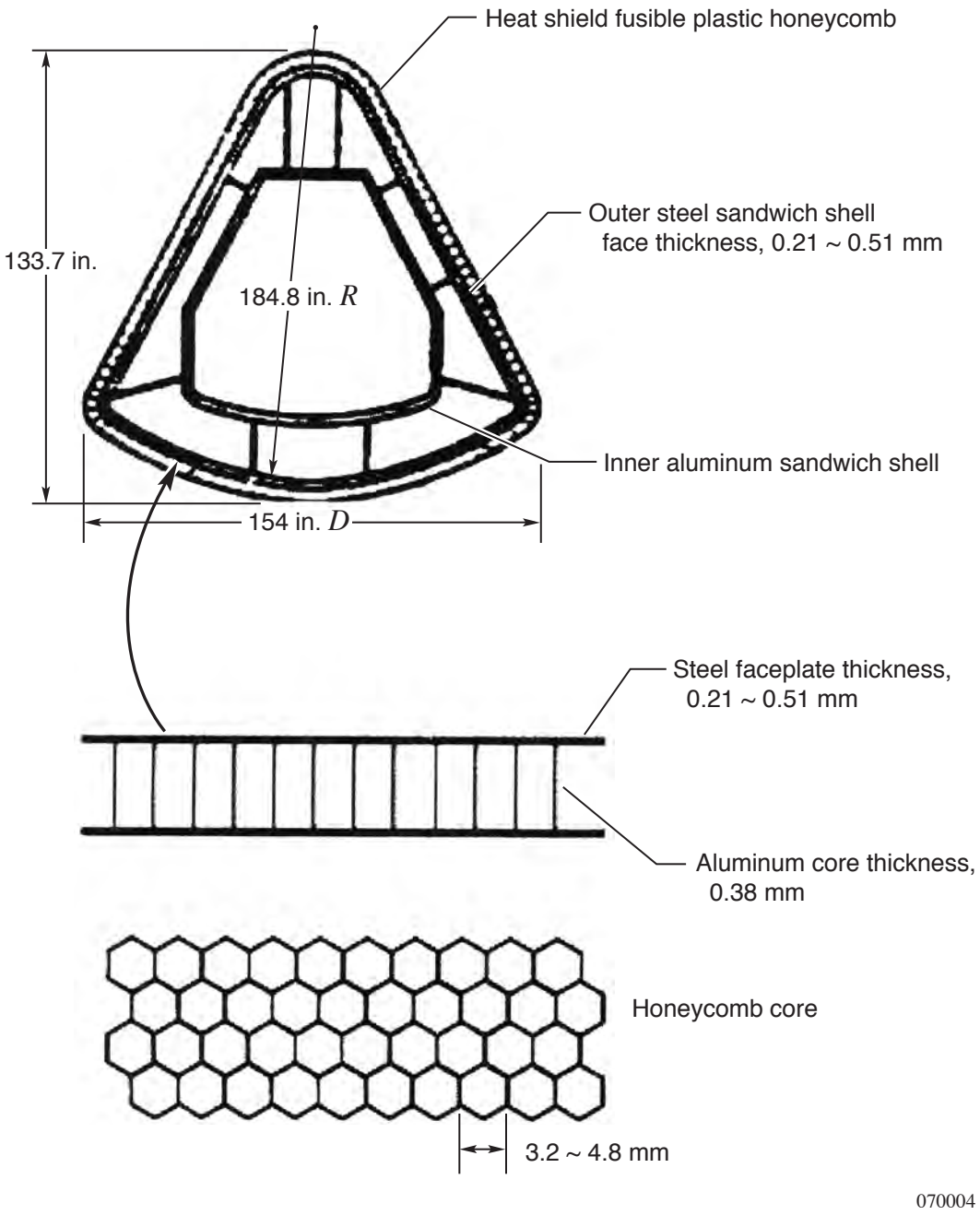

Figure 3. Sandwich construction of the Apollo capsule.

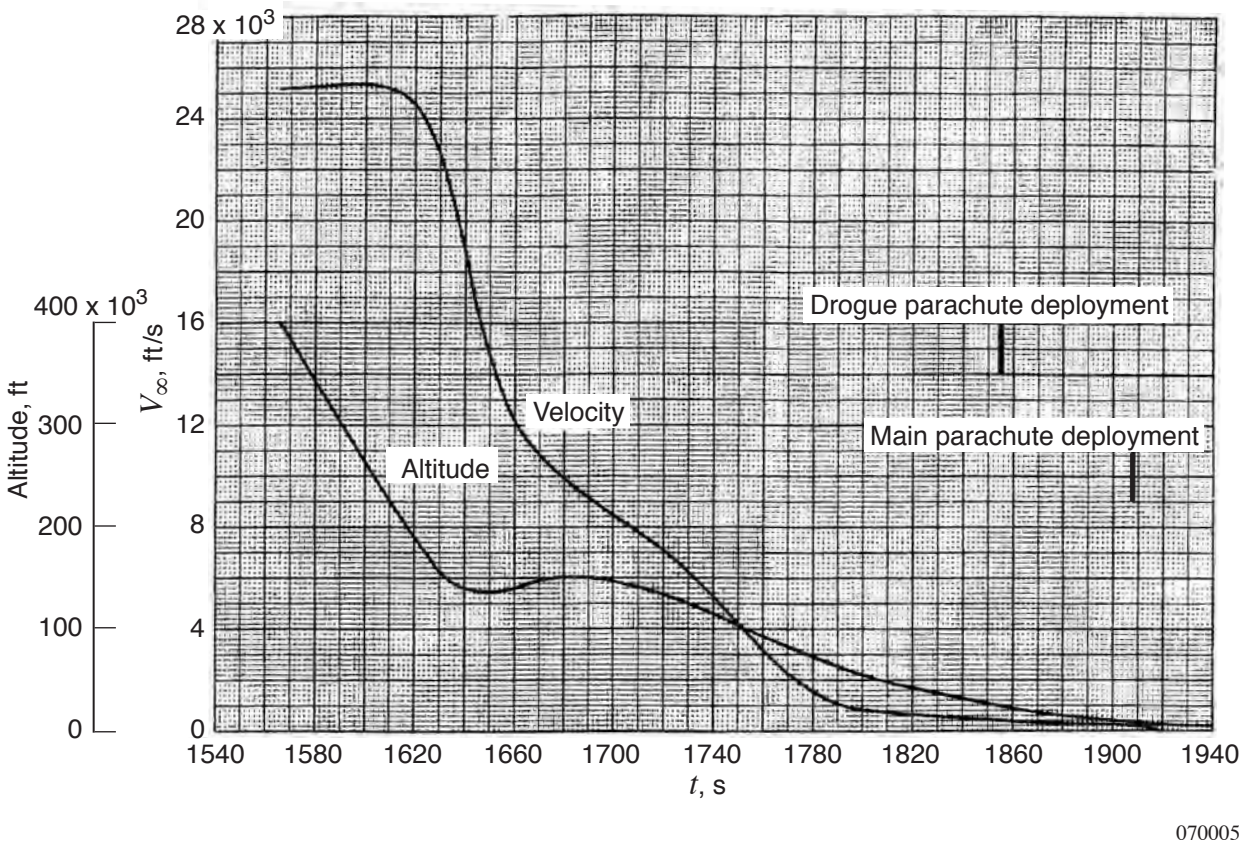

Figure 4. Reentry trajectory of Apollo capsule (ref. 1).

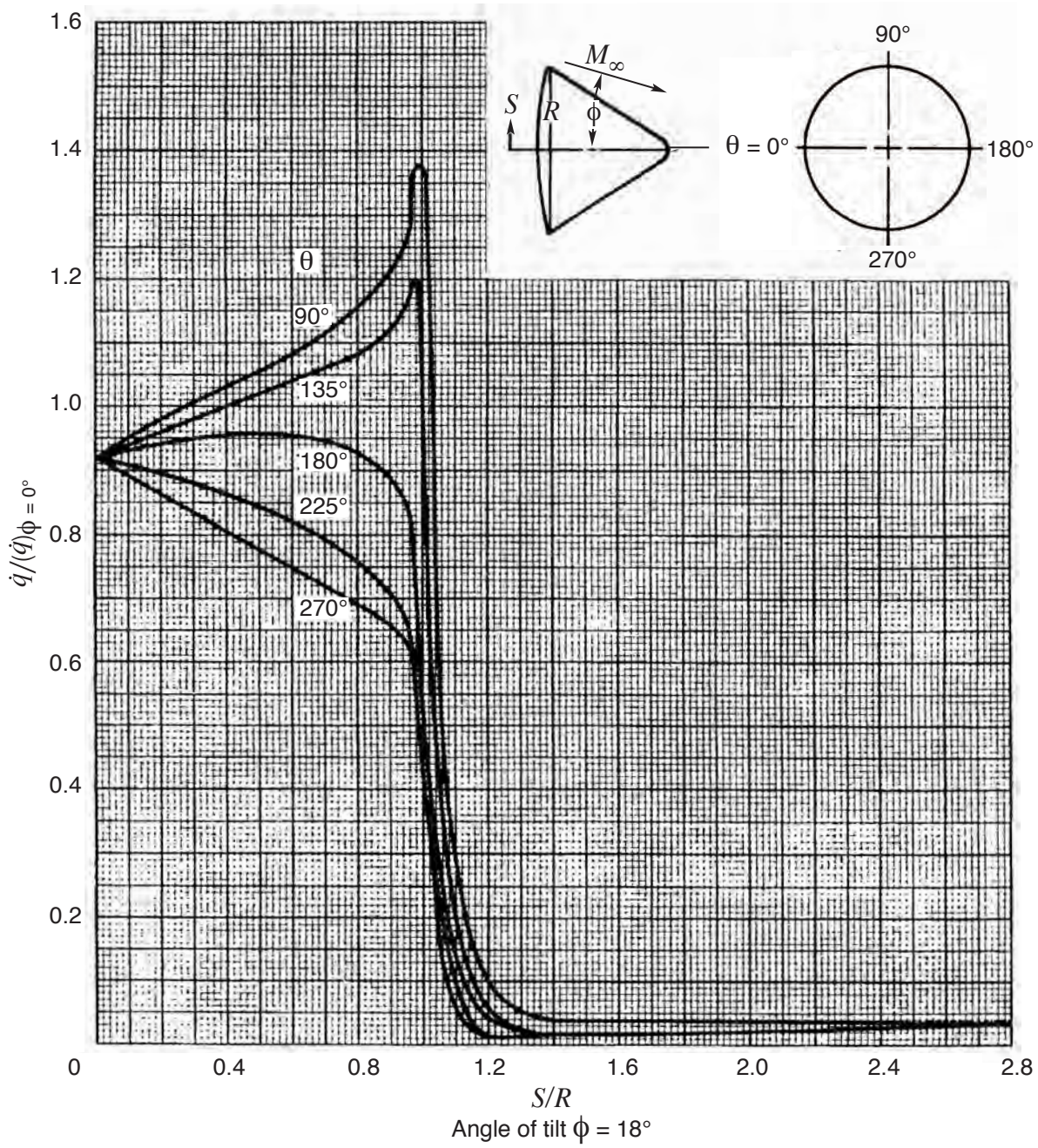

Figure 5. Wind-tunnel distribution of local heating rate for $\phi = 18°$ angle of tilt divided by zero tilt ($\phi = 0°$) stagnation-point heating rate (ref. 1).

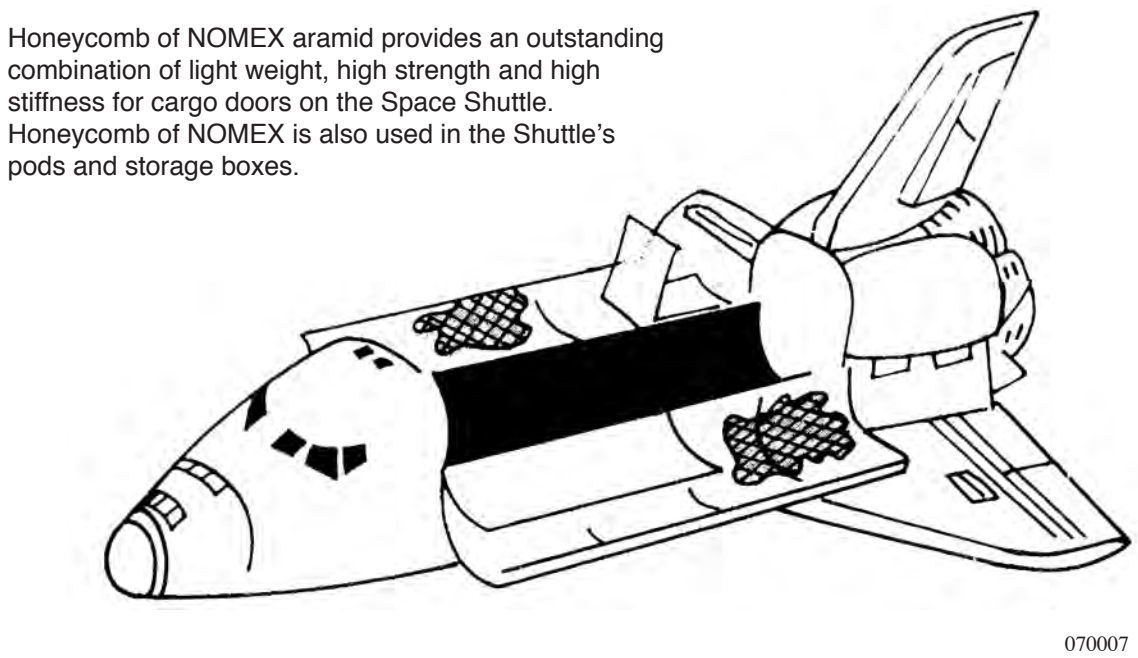

Figure 6. Space Shuttle orbiter cargo bay doors (NOMEX honeycomb core/graphite-epoxy face sheets).

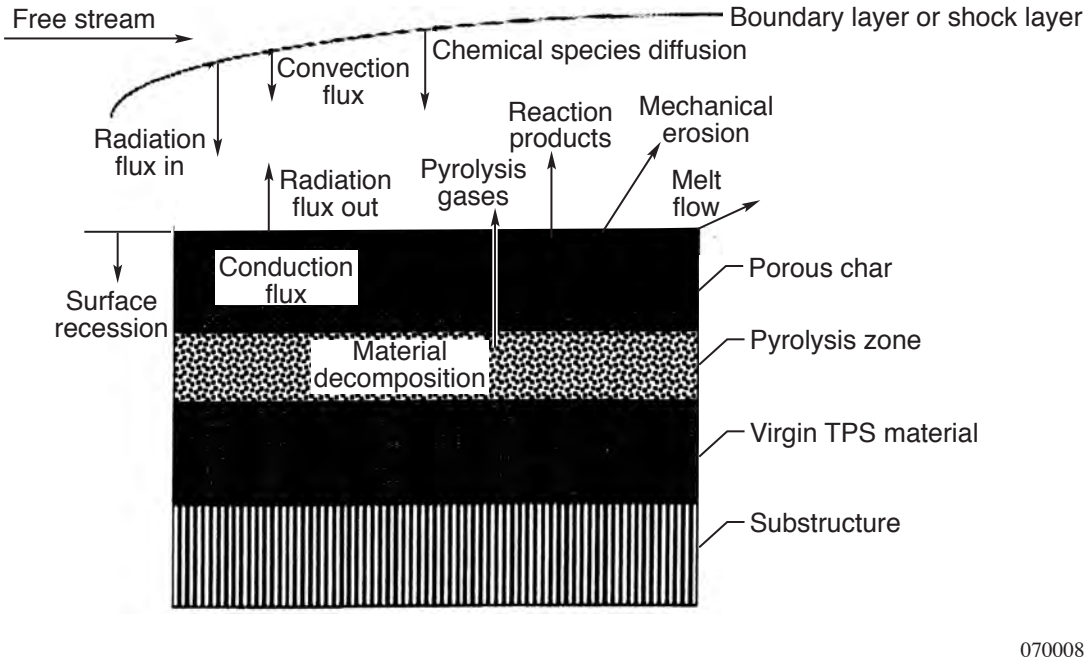

Figure 7. Energy accommodation mechanisms of ablative TPS material (ref. 4).

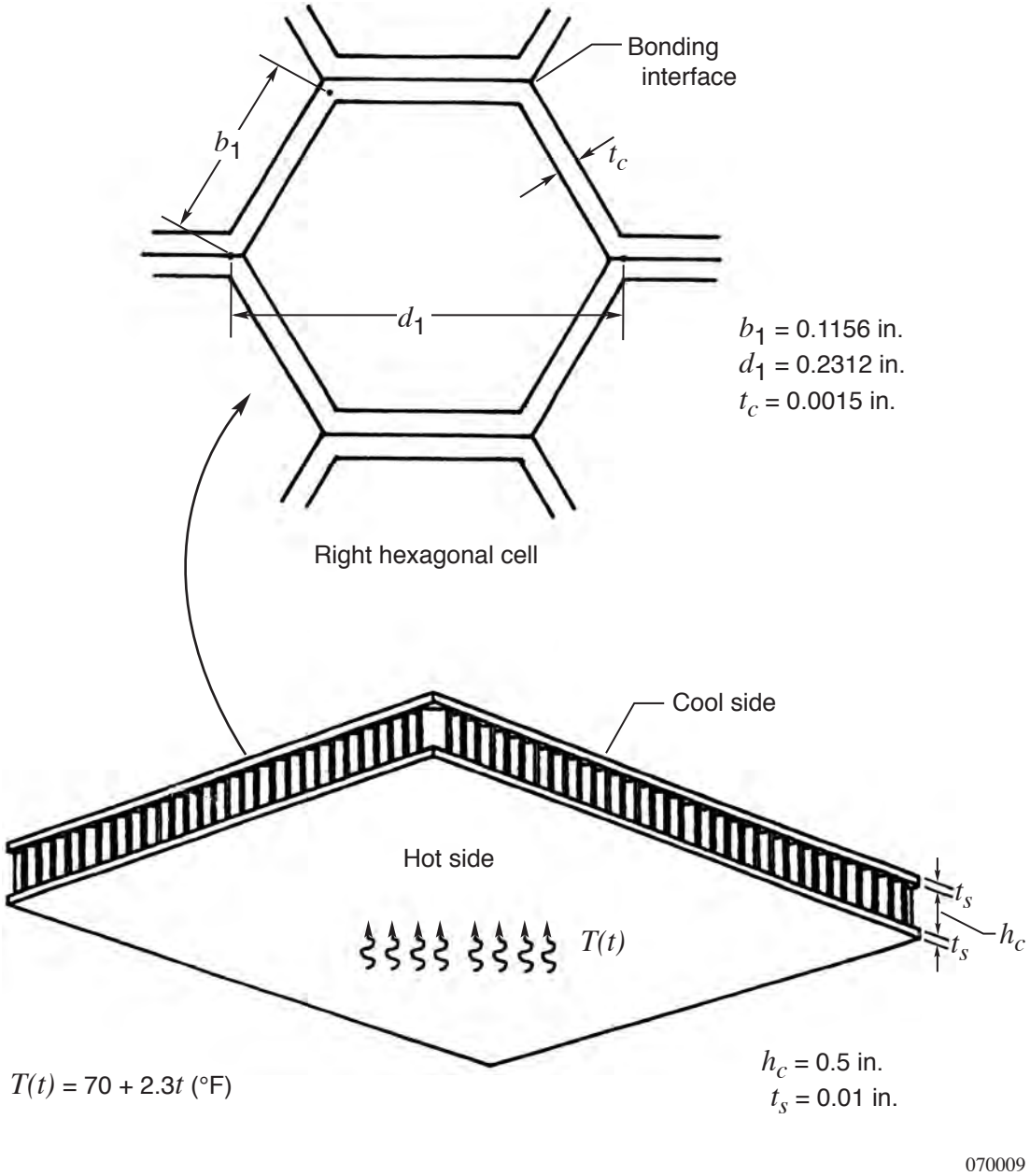

Figure 8. Honeycomb-core sandwich panel subjected to one-sided heating.

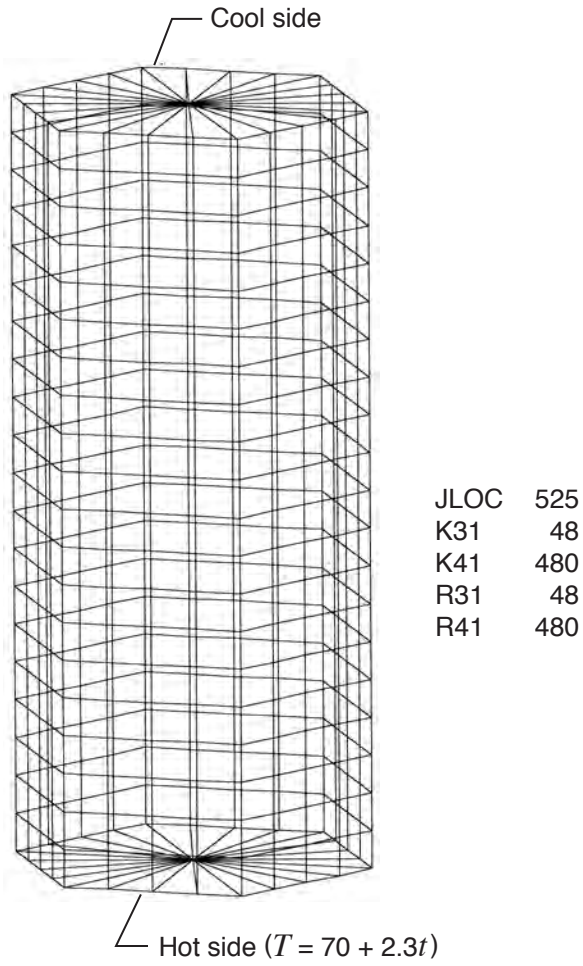

Figure 9(a). Conduction elements.

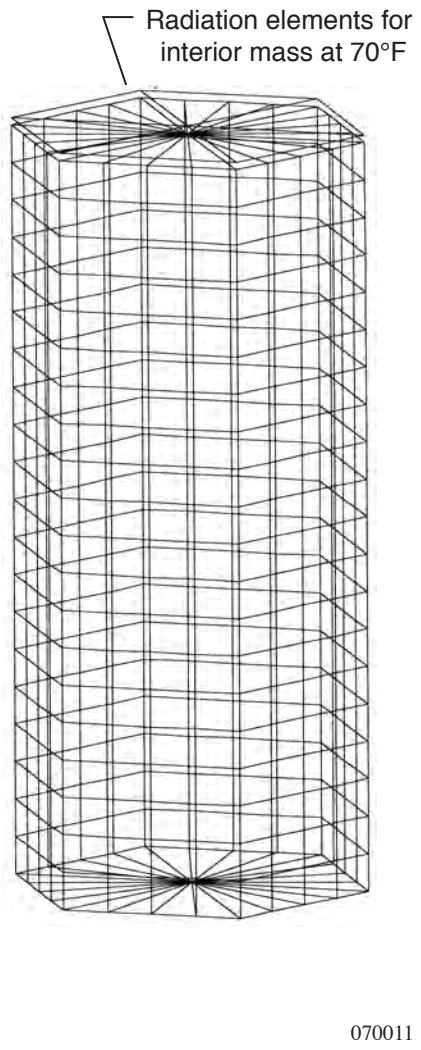

Figure 9(b). Radiation elements.

Figure 9. Thermal models for a hexagonal honeycomb cell.

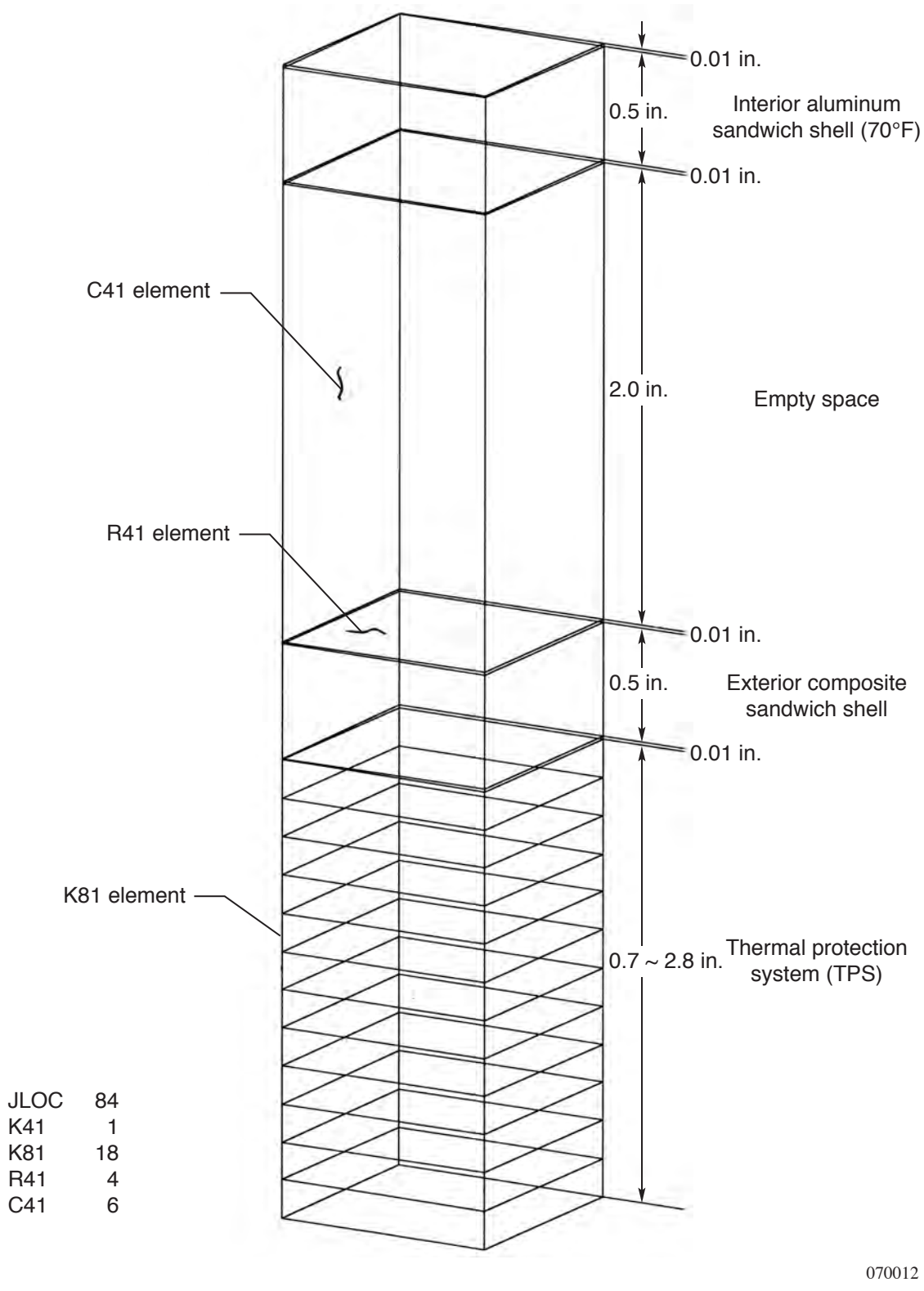

Figure 10. Simple-plug thermal model generated for CEV windward wall.

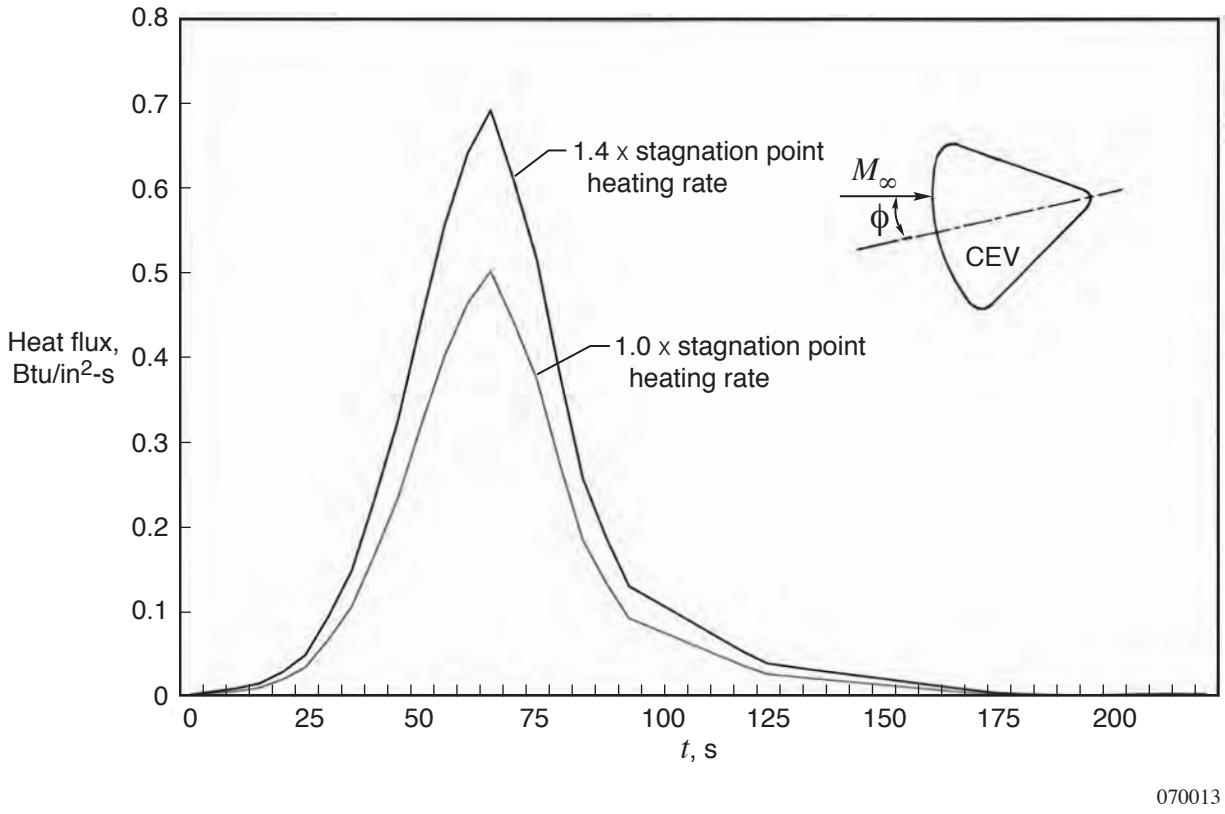

Figure 11. Surface heating rates calculated for CEV stagnation point and toroidal shoulder worst heating point using Apollo reentry trajectories.

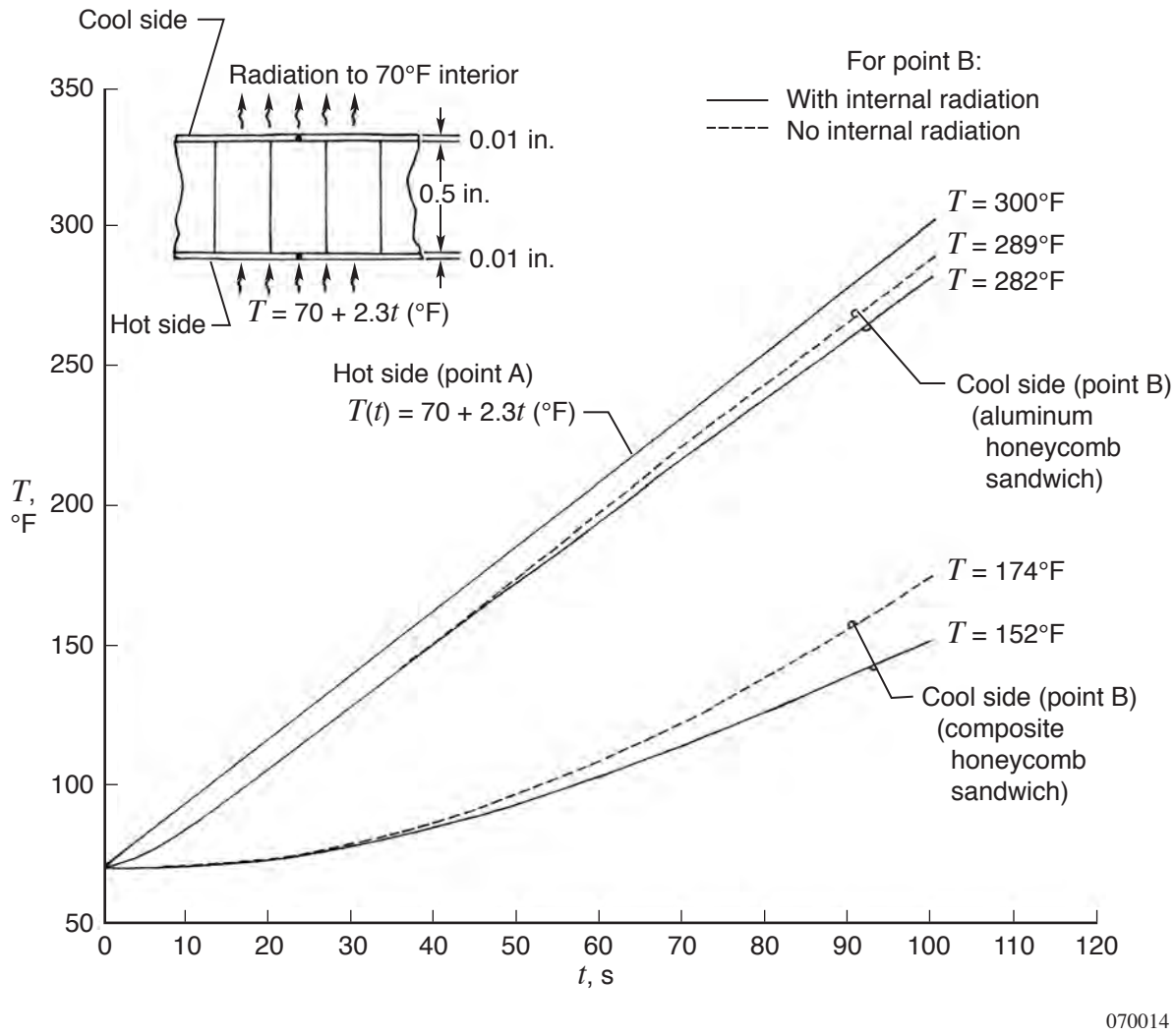

Figure 12. Temperature–time histories at SPAR-calculated inner cool side (point B) of honeycomb-core sandwich panel.

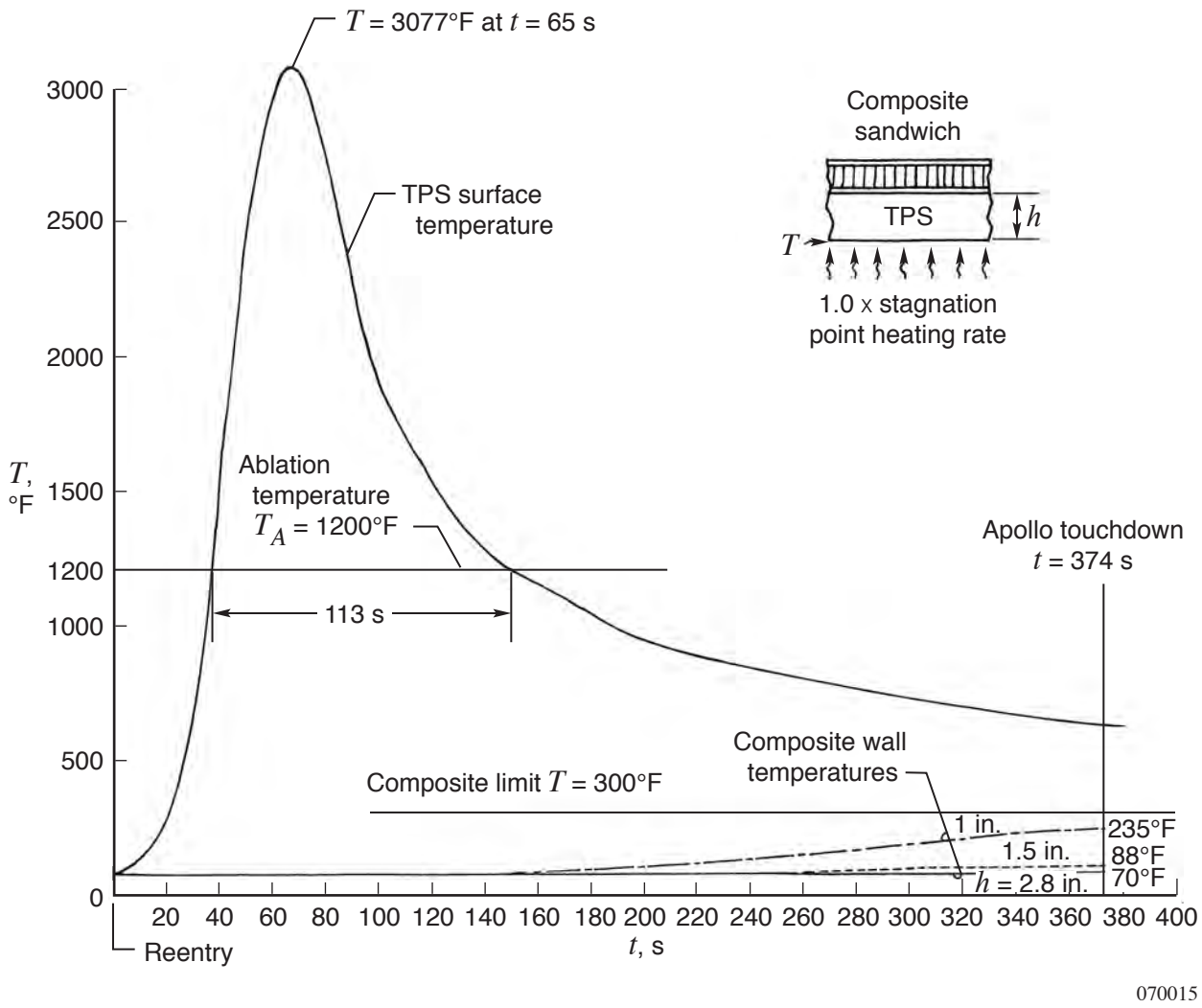

Figure 13. Plots of SPAR-calculated TPS surface temperature and composite sandwich temperatures as functions of time; reentry at $t = 0$ s; 1.0 × stagnation point heating rate.

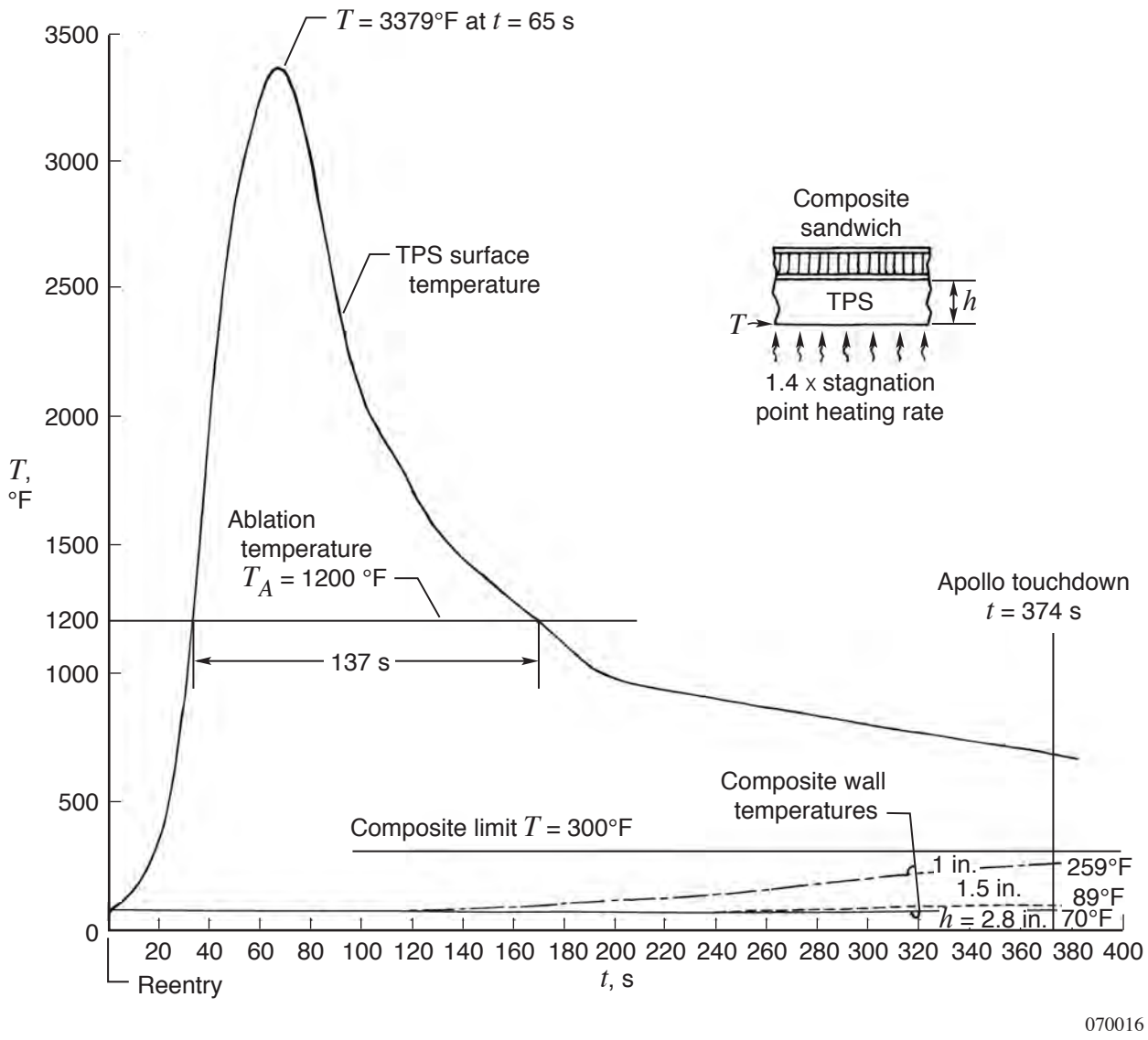

Figure 14. Plots of SPAR-calculated TPS surface temperature and composite sandwich temperatures as functions of time; reentry at $t = 0$ s; 1.4 × stagnation point heating rate.

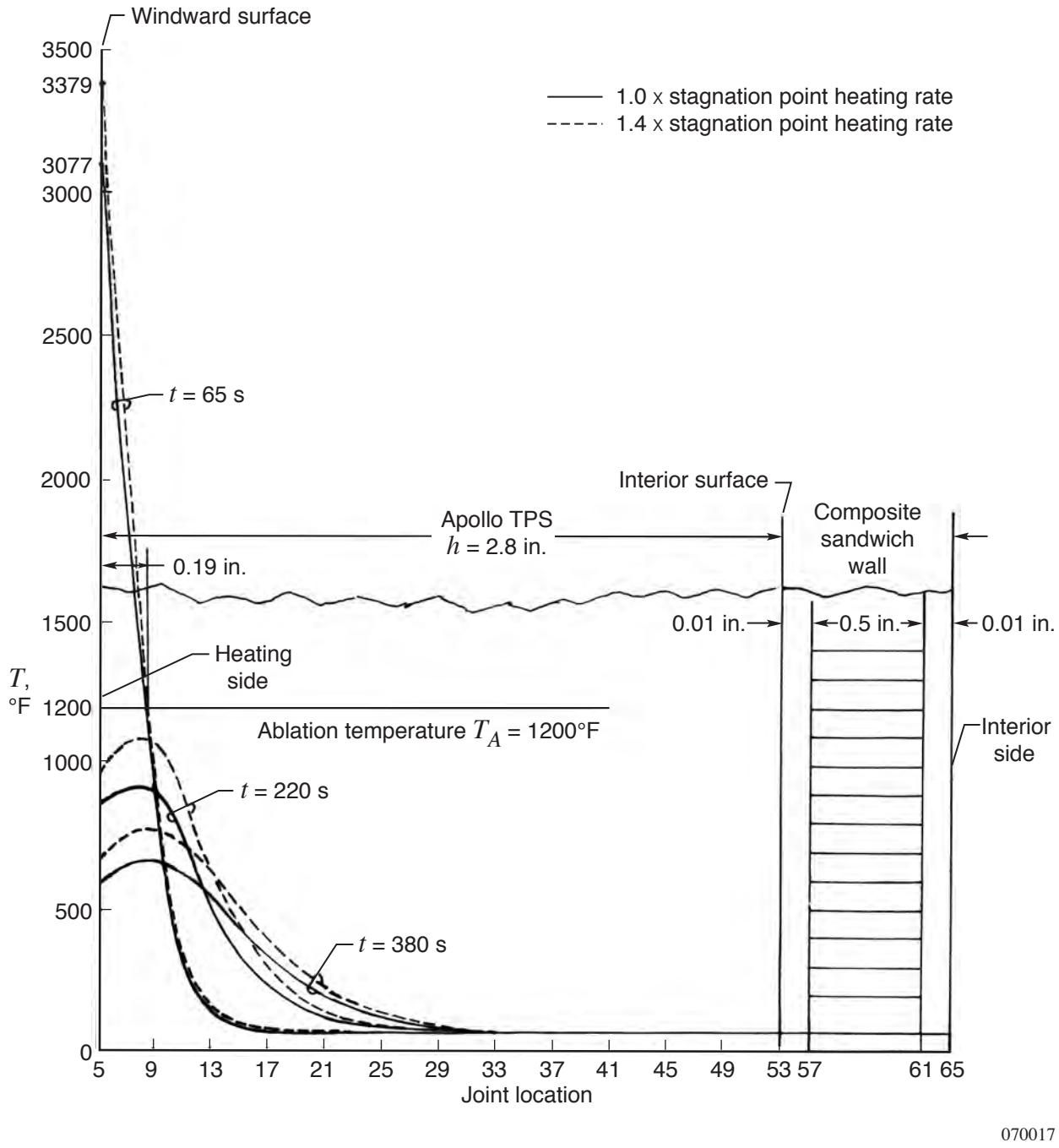

Figure 15. A side view of temperature distributions across the CEV windward wall at different time steps; Apollo TPS thickness h = 2.8 in.

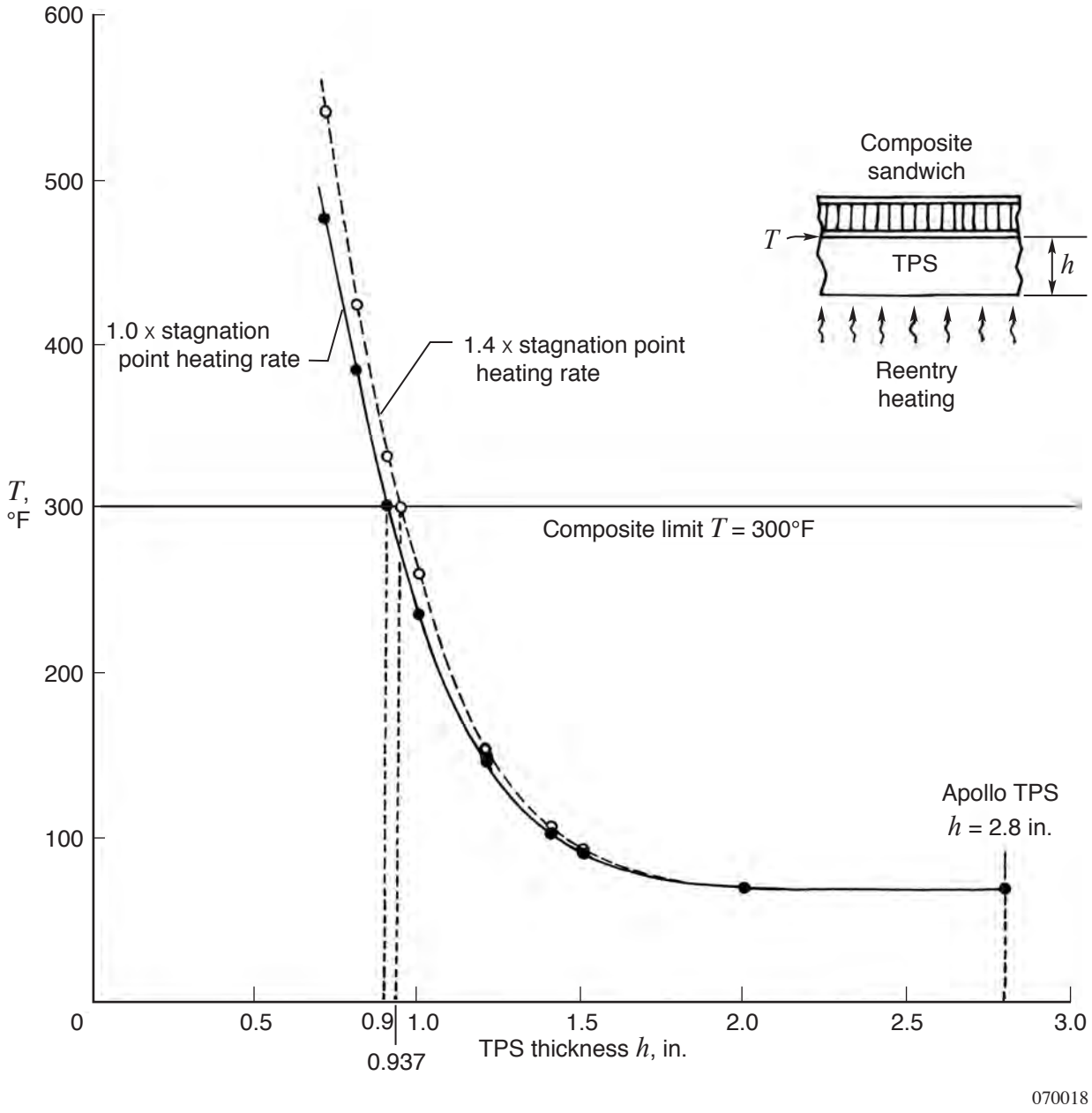

Figure 16. Plots of maximum composite sandwich temperature at touchdown as functions of TPS thickness h; 1.0 × and 1.4 × stagnation point heating rates (nonablation).

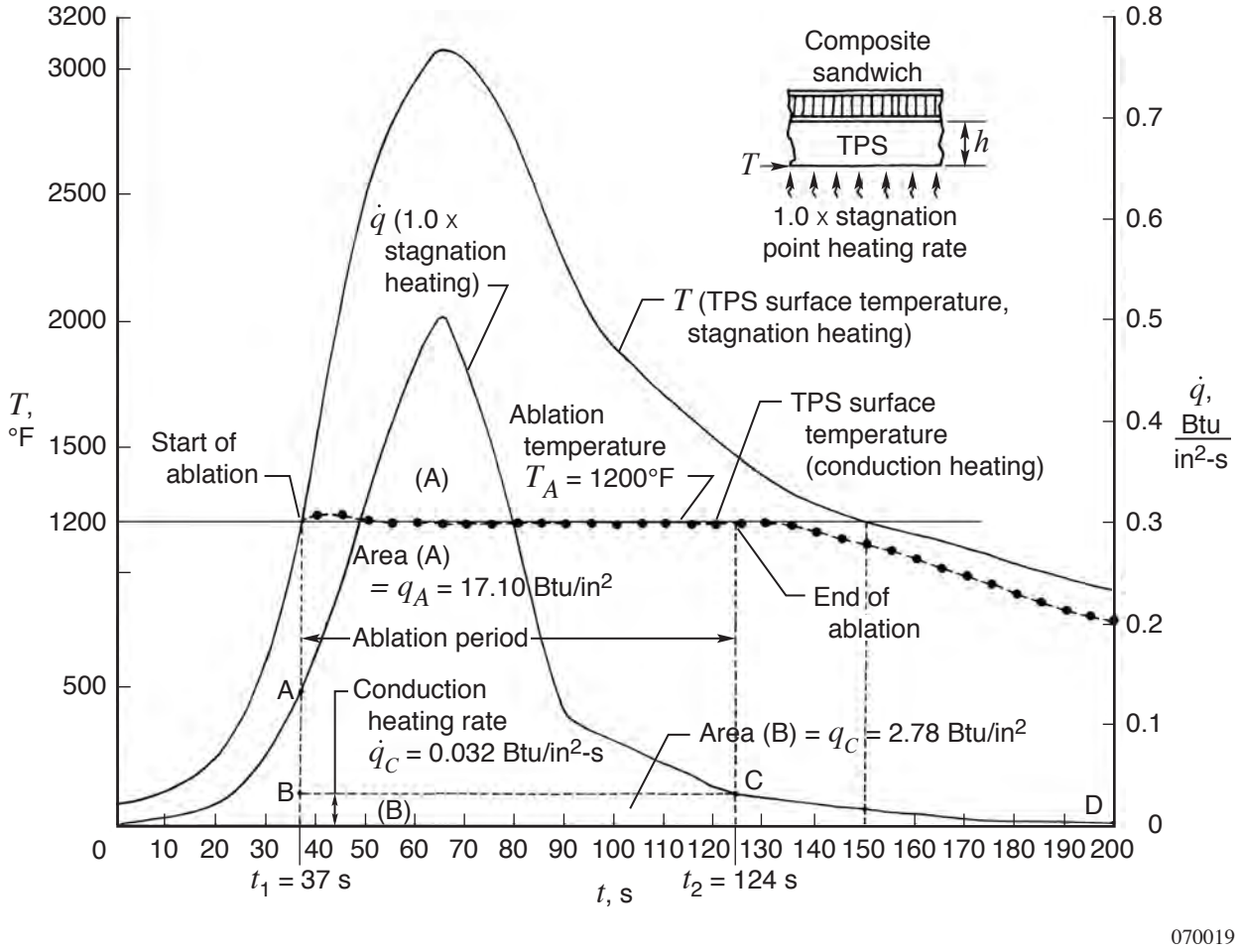

Figure 17. The 1.0 × stagnation point heating curve and associated TPS surface temperature curve for graphical determination of heat load distribution.

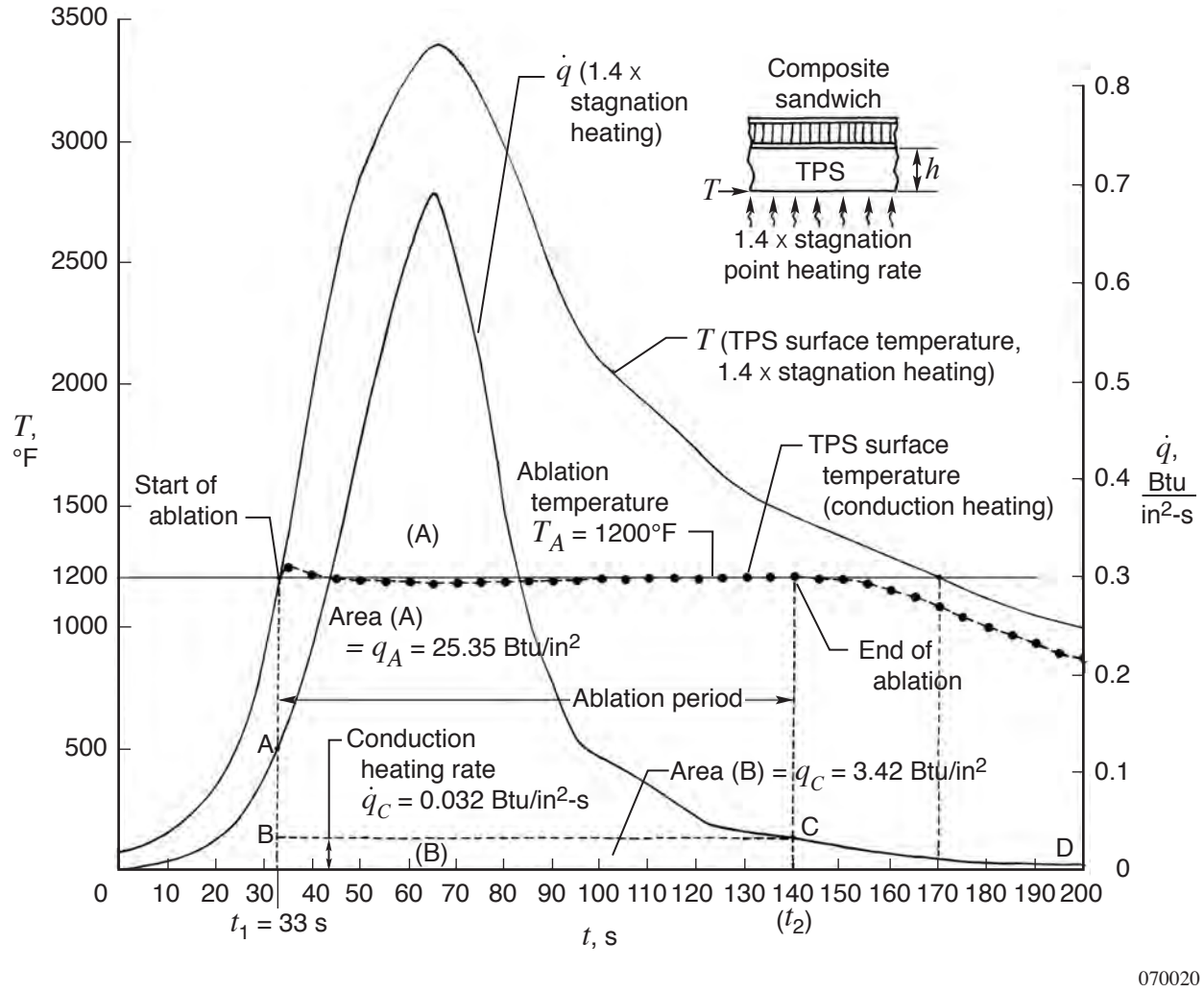

Figure 18. The 1.4 × stagnation point heating curve and associated TPS surface temperature curve for graphical determination of heat load distribution.

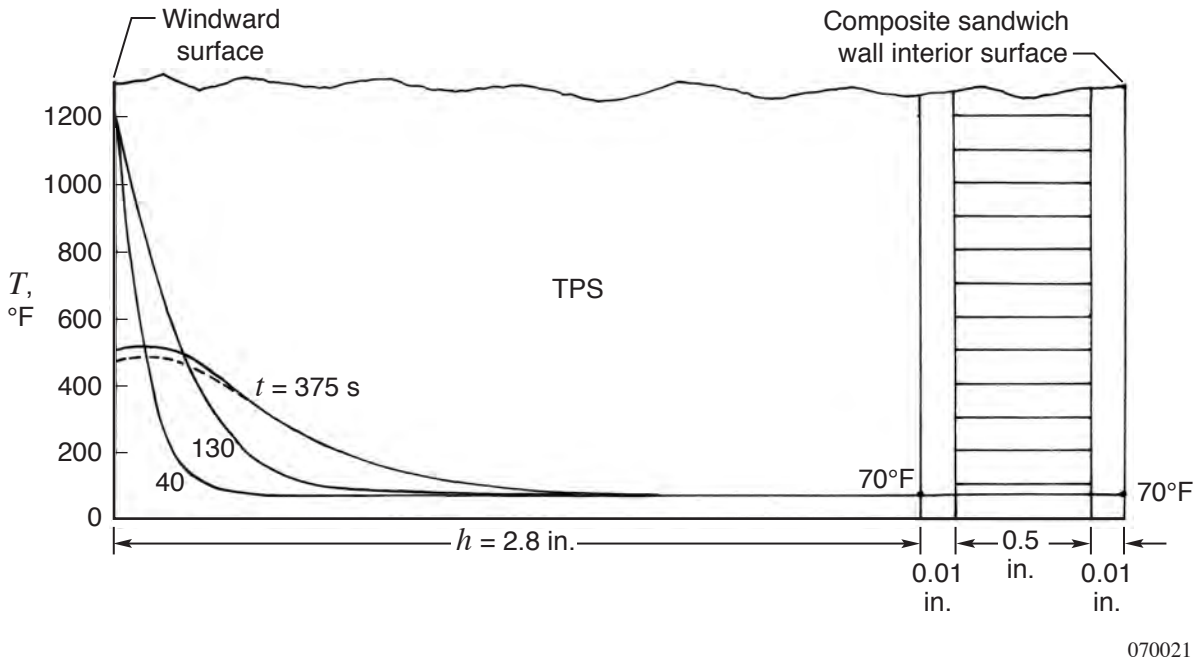

Figure 19(a). TPS thickness h = 2.8 in.

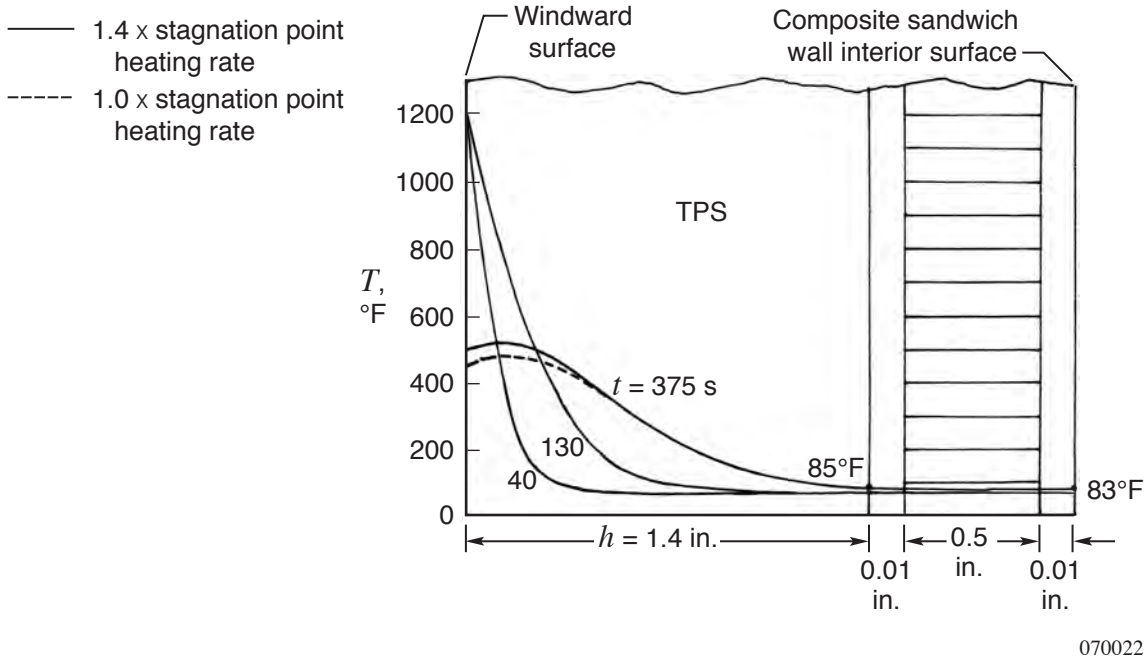

Figure 19(b). TPS thickness h = 1.4 in.

Figure 19. Temperature distributions across the CEV windward wall at different time steps for different TPS thicknesses; conduction heat load.

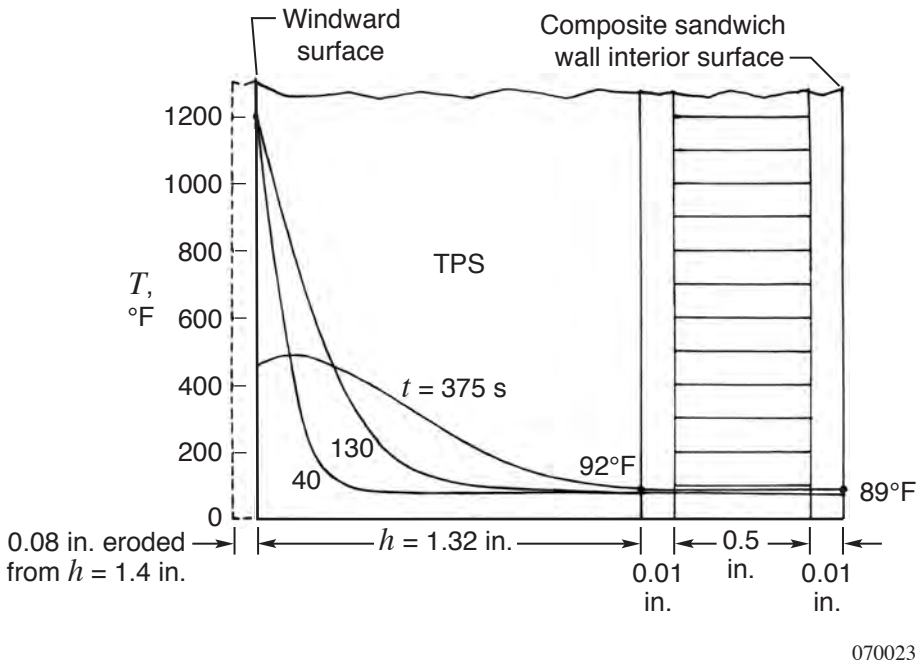

Figure 20. Temperature distributions across the CEV windward wall at different time steps; eroded TPS thickness h = 1.32 in.; 1.0 × stagnation point heating rate.

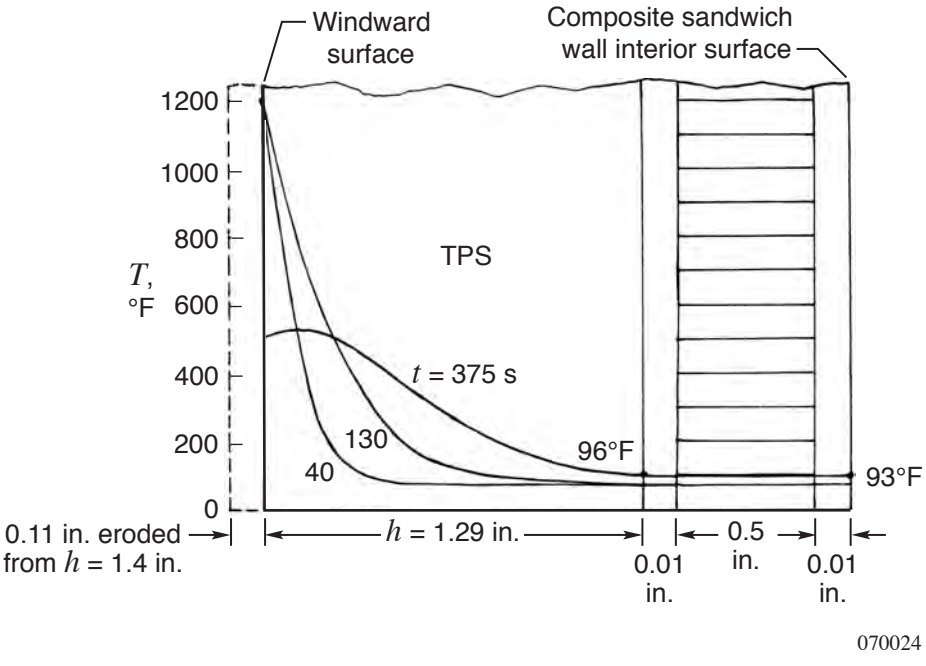

Figure 21. Temperature distributions across the CEV windward wall at different time steps; eroded TPS thickness h = 1.29 in.; 1.4 × stagnation point heating rate.

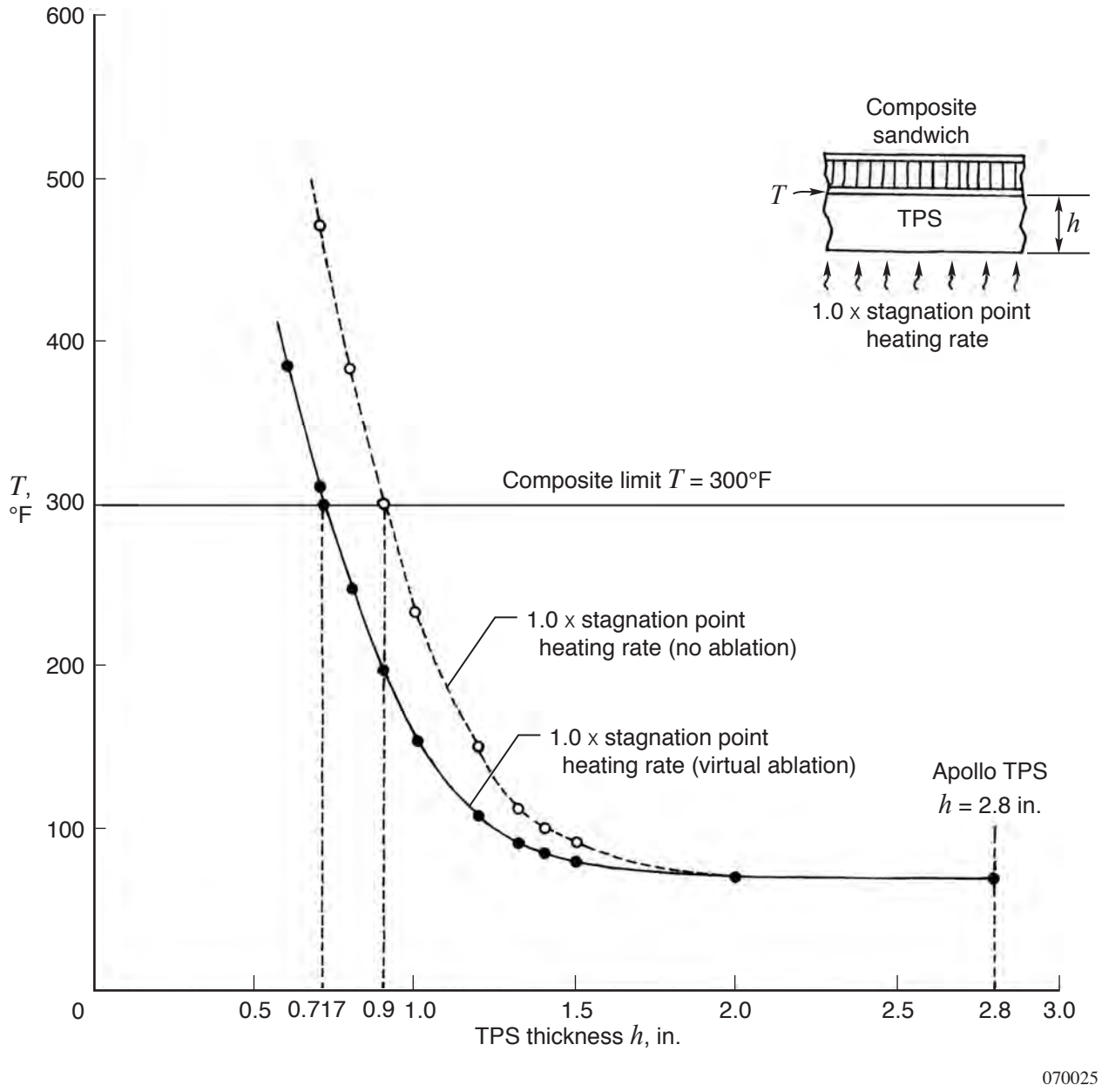

Figure 22. Plots of maximum composite temperatures (at touchdown) as functions of TPS thickness h; 1.0 × stagnation point heating rates.

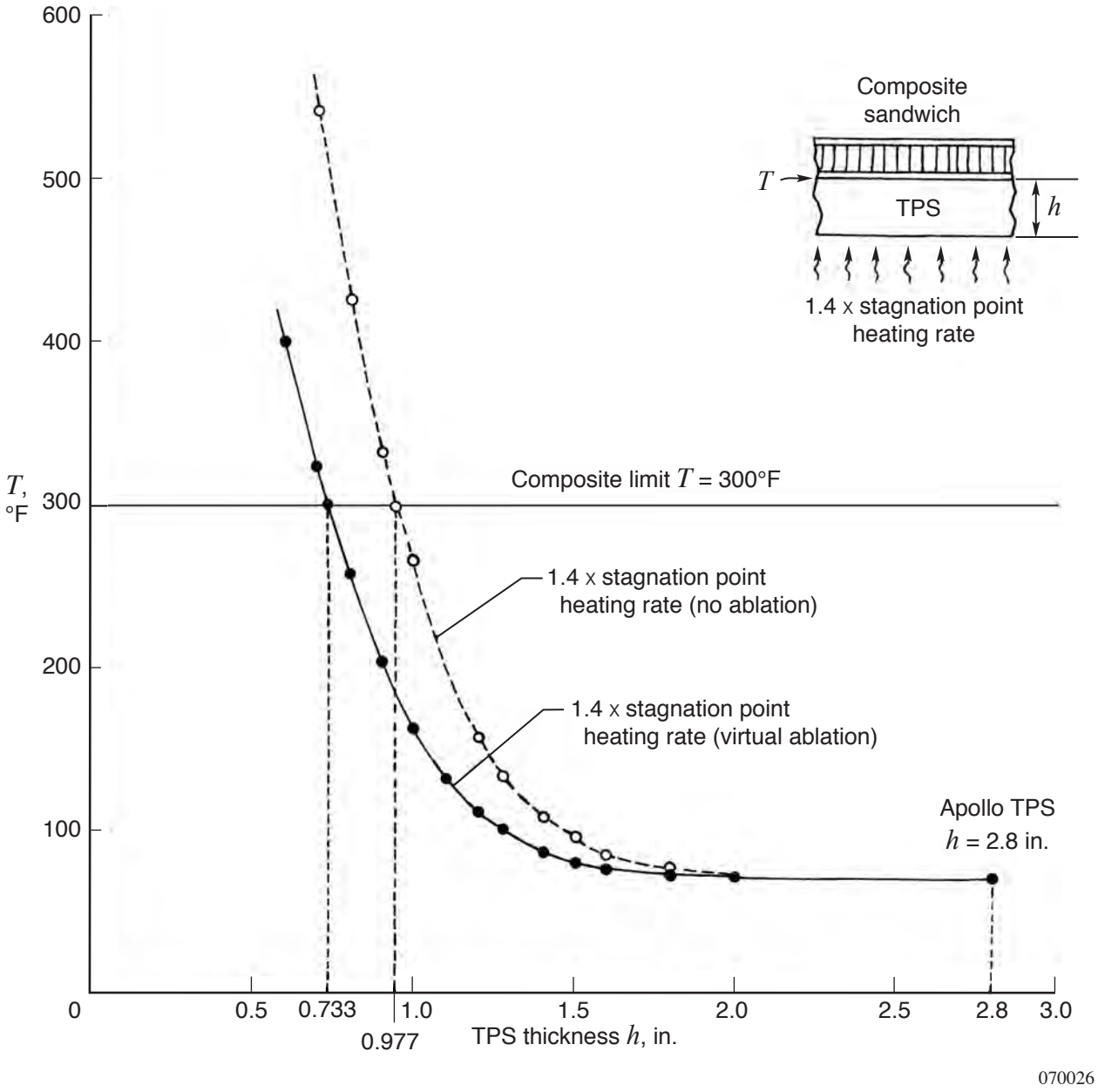

Figure 23. Plots of maximum composite temperatures (at touchdown) as functions of TPS thickness h; 1.4 × stagnation point heating rates.

REFERENCES

1. Lee, Dorothy B., John J. Bertin, and Winston D. Goodrich, *Heat-Transfer Rate and Pressure Measurements Obtained During Apollo Orbital Entries*, NASA TN D-6028, 1970.

2. Ko, William L., *Heat Shielding Characteristics and Thermostructural Performance of a Superalloy Honeycomb Sandwich Thermal Protection System (TPS)*, NASA/TP-2004-212024, 2004.

3. Williams, S. D., and Donald M. Curry, *Thermal Protection Materials; Thermophysical Property Data*, NASA Reference Publication 1289, 1992.

4. Ko, William L., Robert D. Quinn, and Leslie Gong, *Finite-Element Reentry Heat-Transfer Analysis of Space Shuttle Orbiter*, NASA Technical Paper 2657, 1986.

5. Laub, B., and E. Venkatapathy, "Thermal Protection System Technology and Facility Needs for Demanding Future Planetary Missions," presented at the International Workshop on Planetary Probe Atmospheric Entry and Descent Trajectory Analysis and Science, Lisbon, Portugal, October 6–9, 2003.

6. Whetstone, W. D., *SPAR Structural Analysis System Reference Manual; System Level 13A; Volume 1; Program Execution*, NASA-CR-158970-1, 1978.

7. Quinn, Robert D., and Leslie Gong, *A Method for Calculating Transient Surface Temperatures and Surface Heating Rates for High-Speed Aircraft*, NASA/TP-2000-209034, 2000.

REPORT DOCUMENTATION PAGE

Form Approved
OMB No. 0704-0188

1. REPORT DATE *(DD-MM-YYYY)*	2. REPORT TYPE	3. DATES COVERED *(From - To)*
01-05-2007	Technical Memorandum	

4. TITLE AND SUBTITLE
Reentry Thermal Analysis of a Generic Crew Exploration Vehicle Structure

5a. CONTRACT NUMBER

5b. GRANT NUMBER

5c. PROGRAM ELEMENT NUMBER

6. AUTHOR(S)
Ko, William L.; Gong, Leslie; and Quinn, Robert D.

5d. PROJECT NUMBER

5e. TASK NUMBER

5f. WORK UNIT NUMBER

7. PERFORMING ORGANIZATION NAME(S) AND ADDRESS(ES)
NASA Dryden Flight Research Center
P.O. Box 273
Edwards, California 93523-0273

8. PERFORMING ORGANIZATION REPORT NUMBER
H-2674

9. SPONSORING/MONITORING AGENCY NAME(S) AND ADDRESS(ES)
National Aeronautics and Space Administration
Washington, DC 20546-0001

10. SPONSORING/MONITOR'S ACRONYM(S)
NASA

11. SPONSORING/MONITORING REPORT NUMBER
NASA/TM-2007-214607

12. DISTRIBUTION/AVAILABILITY STATEMENT
Unclassified -- Unlimited
Subject Category 34 Availability: NASA CASI (301) 621-0390 Distribution: Standard

13. SUPPLEMENTARY NOTES

14. ABSTRACT

Comparative studies were performed on the heat-shielding characteristics of honeycomb-core sandwich panels fabricated with different materials for possible use as wall panels for the proposed crew exploration vehicle. Graphite/epoxy sandwich panel was found to outperform aluminum sandwich panel under the same geometry due to superior heat-shielding qualities and lower material density. Also, representative reentry heat-transfer analysis was performed on the windward wall structures of a generic crew exploration vehicle. The Apollo low Earth orbit reentry trajectory was used to calculate the reentry heating rates. The generic crew exploration vehicle has a graphite/epoxy composite honeycomb sandwich exterior wall and an aluminum honeycomb sandwich interior wall, and is protected with the Apollo thermal protection system ablative material. In the thermal analysis computer program used, the TPS ablation effect was not yet included; however, the results from the nonablation heat-transfer analyses were used to develop a "virtual ablation" method to estimate the ablation heat loads and the thermal protection system recession thicknesses. Depending on the severity of the heating-rate time history, the virtual ablation period was found to last for 87 to 107 seconds and the ablation heat load was estimated to be in the range of 86 to 88 percent of the total heat load for the ablation time period. The thermal protection system recession thickness was estimated to be in the range of 0.08 to 0.11 inches. For the crew exploration vehicle zero-tilt and 18-degree-tilt stagnation points, thermal protection system thicknesses of h = {0.717, 0.733} inches were found to be adequate to keep the substructural composite sandwich temperature below the limit of 300°F.

15. SUBJECT TERMS
Crew exploration vehicle, Honeycomb walls, Reentry heat transfer analysis, Thermal protection system, Virtual ablation analysis

16. SECURITY CLASSIFICATION OF:			17. LIMITATION OF ABSTRACT	18. NUMBER OF PAGES	19a. NAME OF RESPONSIBLE PERSON
a. REPORT	b. ABSTRACT	c. THIS PAGE			STI Help Desk (email: help@sti.nasa.gov)
					19b. TELEPHONE NUMBER *(Include area code)*
U	U	U	UU	52	(301) 621-0390